Design and Fabrication of a Superprism using 2D Photonic Crystals

by

Sheila Tandon

B.E. Electrical Engineering
Cooper Union 1999

Submitted to the Department of Electrical Engineering and Computer Science in partial fulfillment of the requirements for the degree of

Master of Science in Electrical Engineering

at the
MASSACHUSETTS INSTITUTE OF TECHNOLOGY

June 2002

© 2002 Massachusetts Institute of Technology. All rights reserved.

Author ....
Sheila Tandon
Department of Electrical Engineering and Computer Science
May 10, 2002

Certified by ....
Leslie A. Kolodziejski
Professor of Electrical Engineering and Computer Science
Thesis Supervisor

Accepted by ....
Arthur C. Smith
Chairman, Department Committee for Graduate Students

Design and Fabrication of a Superprism using 2D Photonic Crystals

by

Sheila Tandon

Submitted to the Department of Electrical Engineering
and Computer Science on May 10, 2002 in partial fulfillment
of the requirements for the degree of
Master of Science in Electrical Engineering

ABSTRACT

A superprism is an optical device which enhances the effects of a conventional prism in two ways: it disperses multiple wavelengths of light and allows for highly sensitive steering of a single wavelength beam over much wider angles than in a conventional prism. Photonic crystals offer an exciting new approach to the problem of wide angle light dispersion and beam steering using a compact solution with no mechanical elements. Being able to realize the superprism effects of photonic crystals would be very useful for a number of applications ranging from enhanced devices for wavelength division multiplexed (WDM) systems to a new class of ultra-refractive optical elements for beam manipulation.

For this Master's Thesis research, a superprism device is designed using the "superprism" effects of a two dimensional photonic crystal. A fabrication approach is then outlined, and all processing steps are investigated. The device design is scalable with the wavelength of operation. In our fabrication approach, we aim for a large scale device (2 cm x 2 cm) with an operating wavelength of 3 μm. This wavelength implies a photonic crystal period of 750 nm and a hole radius of 300 nm. The photonic crystal is patterned using interference lithography followed by reactive ion etching of a GaAs/AlGaAs epilayer, and a large scale oxidation to create a low refractive index Al_xO_y layer.

Thesis Supervisor: Leslie A. Kolodziejski
Professor of Electrical Engineering and Computer Science

Acknowledgements

The work presented here, though written by me, is the compilation of the efforts of many people who guided and supported me along the way.

Thank-you Alexei Erchak for really getting me started in the lab. Thank-you for being patient with me and always being there to listen when I need an "older" student's advice. I'll try to keep my nitrogen gun pointing in the right direction from now on. Thank-you Chiyan Luo for working so well with me on our many design issues. Thank-you Professor Hank Smith and the guys in the Nanostructures Laboratory for teaching me everything about making really, really, small things. Mike Walsh, Tim Savas, Jim Daley, Jimmy Carter, thank-you for all the time you've generously spent with me as I've learned my way around the lab. Thank-you Gale Petrich for humoring my questions and giving me pointers in the right direction. Thank-you Solomon Assefa, Ryan Williams, Reggie Bryant, and Aleksandra Markina for always being the friendly and helpful group mates that you are.

Thank-you Professor Leslie Kolodziejski for being the guiding hand for me along the way. I said I wanted to do something new in optics and you openly welcomed me into your group. Thank-you for your unwavering support and encouragement as I navigate my way through the difficulties of MIT. I'm happy to know that you are always on my side.

I especially want to thank my parents and my brother and sisters who have always supported my decision to study at MIT. Though I am not sure where this path is leading me, your love and encouragement have kept my spirit alive. Last but not least, I must thank Sorin Misa for being my #1 fan, my perennial source of laughter, and my very best friend through it all.

They said they couldn't imagine me in a lab coat. I guess that was because they never saw me in a bunny suit!

Thank-you to everyone who believed in me.

Table of Contents

ABSTRACT 3
1.0 INTRODUCTION 13
2.0 DESIGN THEORY & SIMULATION 16
2.1 How can we make a prism "super"? 16
2.2 What are Photonic Crystals? 19
2.3 Superprism Design and Simulation 22
3.0 RESEARCH APPROACH 28
3.1 Research Objective 28
3.2 Design Tolerances 28
3.3 Fabrication Sequence 30
4.0 DISCUSSION & RESULTS 35
4.1 Molecular Beam Epitaxy Results 35
4.2 Photolithography Results 36
4.3 Interference Lithography Results 37
4.3.1 Basic Overview of Interference Lithography 37
4.3.2 The Lloyd's Mirror Interferometer 38
4.3.3 The Two Beam Interferometer 39
4.3.4 Fabricating Photonic Crystal Grids 40
4.3.5 Future Work 42
4.4 Substrate Preparation 42
4.4.1 Trilayer Resist Stack 42
4.4.2 Hard Mask Preparation 44
4.4.3 Future Work 44
4.5 Reactive Ion Etching Results 45
4.5.1 Tri-layer and hard mask etching results 45
4.5.2 Future Work 52
4.6 Oxidation Results 53
4.6.1 Oxidation Experiments 53
4.6.2 Future Work 56
5.0 CONCLUSION 57
6.0 REFERENCES 58

List of Figures

FIGURE 1.1 Illustration of the "super-dispersion" property of a superprism versus dispersion in a conventional prism. For a smaller range of wavelengths, the dispersion in a superprism is much stronger [1]. 13

FIGURE 1.2 Illustration of ultra-refraction in a superprism. A small swing in the incident angle results in a large swing in the output angle. 14

FIGURE 2.3 (a) The dispersion surface of an arbitrary isotropic medium showing the direction of the k-vector and the direction of power propagation [4]. (b.) The dispersion surfaces for multiple frequencies in an isotropic medium. Each frequency has a dispersion surface of a different radius.......... 16

FIGURE 2.4 The dispersion surfaces of a uniaxial medium showing the difference in the direction of the k-vector versus the direction of power propagation for the extraordinary wave [4]. .. 17

FIGURE 2.5 The dispersion surfaces on each side of a boundary between air and a higher index material. 17

FIGURE 2.6 Superprism effects using large changes in the group velocity. (a) Illustration of angular magnification at a constant frequency in a superprism. (b) Illustration of super-dispersion in the superprism. 18

FIGURE 2.7 Highly dispersive effects using differences in phase velocity.......... 19

FIGURE 2.8 From left to right, examples of (a) one, (b) two, and (c) three dimensional photonic crystals. The different colors represent materials of different dielectric constants [5]. 20

FIGURE 2.9 Sketches of photonic band structures for propagation perpendicular to the plane of a 1D photonic crystal made of stacked dielectric slabs as in Figure 2.8(a). (a) Band structure with slabs having the same index of refraction. (b) Band structure with slabs alternating between high and low refractive index materials. The high index contrast creates a band gap in allowed frequencies for this case [5]. 20

FIGURE 2.10 Superprism device schematic (not to scale). 22

FIGURE 2.11 Dispersion surface calculation for photonic crystal design. The square lattice orientation is shown in the inset [7]. 23

FIGURE 2.12 The band structure for the superprism photonic crystal [7]. 24

FIGURE 2.13 Explanation of Superprism ultra-refraction using the dispersion surfaces in the photonic crystal and GaAs [7]. 24

FIGURE 2.14 Time domain simulation of superprism ultra-refraction. The simulation was performed on a simplified 2D structure which did not consider the effects of a finite device thickness [7]. 26

FIGURE 3.1 Superprism device tolerances.......... 29

FIGURE 3.2 Growth of epilayer, sputtering of SiO_2 and Cr evaporation.......... 30

FIGURE 3.3 Photolithography mask design schematic. Mask 1 and Mask 2 are two 4” masks with the chrome pattern on glass (mask outline not shown). 31

FIGURE 3.4 Photolithography with Mask 1 31

FIGURE 3.5 Interference Lithography with use of trilayer resist stack. Please see Chapter 4 for a discussion of thicknesses. 32

FIGURE 3.6 Reactive Ion Etching of trilayer resist stack and SiO_2 hard mask. The deep holes shown are only to illustrate pattern transfer through each layer. As the hole pattern is transferred through each layer, layer thicknesses decrease due to sputtering and etching thus avoiding unnecessary high aspect ratio etching. 33

FIGURE 3.7 Photolithography using Mask 2.. 33

FIGURE 3.8 Reactive ion etch substrate and oxidize AlAs layer 34

FIGURE 4.1 A scanning electron microscope (SEM) image of a randomly fractured edge of the GaAs heterostructure showing the GaAs/AlGaAs/AlAs epilayer on the GaAs substrate. The 50nm AlGaAs layers are not clearly visible due to the non uniformity of the surface. 35

FIGURE 4.2 Photolithography mask designs: Mask 1 (left) and Mask 2 (right). 2” Wafer outline and cross-hairs are for reference and will not be exposed. Cross and circle-shaped alignment marks are used to align the patterns from Mask 2 to the pattern exposed on the wafer using Mask 1.. 36

FIGURE 4.3 In interference lithography, the standing wave formed by the interference of two light beams exposes a periodic grating on the substrate. In this schematic, the incoming waves are approximated as plane waves when in reality they are spherical. 37

FIGURE 4.4 Top view of the Lloyd's mirror interferometer system showing light incident upon the mirror and substrate simultaneously. The light reflected off the mirror interferes with the light directly incident upon the substrate to form a periodic pattern. The rotation stage sets the period by changing the orientation of the mirror and substrate........................... 38

FIGURE 4.5 A grating pattern in resist exposed using the Lloyd's mirror interferometer. The period is approximately 760 nm. 38

FIGURE 4.6 The two beam Interference Lithography system used in the Nanostructures Laboratory. 39

FIGURE 4.7 Examples of grid exposures using the Lloyd’s mirror for different exposure times. Grids are exposed in PFI 88 positive resist on silicon for (a) 2 min (b) 2min 24sec (c) 2 min 48 sec (d) 3 min 12 sec per side (the total exposure time is double). The period is approximately 750 nm for every case. 41

FIGURE 4.8 Examples of grid exposures in negative resist using the Lloyd’s mirror for different exposure times. Grids are exposed in OKHA negative resist on silicon for (a) 1 min (b) 1 min 20 sec (c) 1 min 40 sec (d) 2 min per side (the total exposure time is double). The period is approximately 750 nm for every case... 41

FIGURE 4.9 Reflectivity profile for layered medium consisting of 200nm PFI-88 positive resist, 90nm SiO_2, BARLi ARC, 250nm SiO_2, GaAs substrate. 43

FIGURE 4.10 Exposure of grid pattern using the Lloyd's mirror interferometer. (a) Grid pattern in resist with 90nm SiO_2 interlayer, 300nm ARC, and 250 SiO_2 hard mask layer on a GaAs substrate. (b) Grid pattern in the SiO_2 hard mask layer after reactive ion etching of the trilayer resist stack. A thin layer of ARC remains on top. 44

FIGURE 4.11 SEM image after an Interference Lithography exposure using the Lloyd’s mirror interferometer. The 750 nm period hole pattern is in about 200 nm of positive resist with a 20 nm SiO_2 interlayer, 200 nm ARC layer, and 100 nm SiO_2 hard mask layer on a GaAs substrate. 45

FIGURE 4.12 SEM image showing holes in SiO_2 and ARC. The SiO_2 hard mask layer remains unetched. The 20 nm SiO_2 interlayer was etched using CHF_3(10 mT, 100V, 190W, 1:10) and the 200 nm ARC layer was etched using He/O_2(2:1 sccm, 10 mT, 250 V, 330 W, 1:40). 46

FIGURE 4.13 SEM image after incomplete etching of the 100 nm SiO_2 hard mask layer using the ARC as a mask with CF_4 (10 mT, 100V, 180 W, 2:40). About 20 nm of the SiO_2 layer remains to be etched implying an etch rate of ~30 nm/min. About 95 nm ARC remains of the original 200 nm implying an etch rate of ~40 nm/min. 47

FIGURE 4.14 SEM image after etching the SiO_2 hard mask layer and He/O_2 ashing to remove the remaining ARC. 47

FIGURE 4.15 Detail of a Lloyd’s mirror exposure with trilayer resist stack and SiO_2 hard mask layer on a GaAs substrate. 48

FIGURE 4.16 Etching the SiO_2 hard mask layer using 1:1 CF_4/CHF_3 49

FIGURE 4.17 Etching of the SiO_2 hard mask layer using CHF_3. 50

FIGURE 4.18 A 500nm SiO_2 hard mask layer after He/O_2 ashing the ARC layer 50

FIGURE 4.19 Results of a GaAs etch using BCl_3 (20sccm, 10mT, 60W, 500V, 20:00) with a 500 nm SiO_2 etch mask [9]. 51

FIGURE 4.20 Results of a GaAs etch using BCl_3 (15sccm, 10mT, 60W, 500V, 10:00) with a 160 nm SiO_2 etch mask [9]. 52

FIGURE 4.21 Oxidation setup showing quartz tube which carries water vapor and N_2 into an elevated temperature furnace. 53

FIGURE 4.22 Top view of superprism device shape showing the longest distance from the device edge to the photonic crystal area of ~6mm. This distance implies that the longest distance for oxidation is about half, or ~3mm. 54

FIGURE 4.23 Top view of GaAs/AlAs heterostructure illustrating delamination after an oxidation experiment at 400ºC. The delamination is shown here as a buckling of the GaAs epilayer. The structure was 450 nm GaAs, 50 nm $Al_{0.50}Ga_{0.50}As$, 3000 nm AlAs, 50 nm $Al_{0.50}Ga_{0.50}As$ on a GaAs substrate.. 55

1.0 INTRODUCTION

A prism is an optical element which is used to refract or disperse a beam of light. Prisms are usually made from a uniform material such as glass bounded by non-parallel planes. As light travels through a prism, it bends according to the index of refraction of the material. If we change the direction of the incident light, the beam emerging from the prism also changes direction. At the same time, if a broad spectrum of light is incident on the prism, each color exits the prism in a different direction forming a “rainbow.” Therefore by changing the color of the beam we can change the direction the beam travels through a prism.

In a conventional prism, these directional changes are small. Changing the direction of an incident beam introduces only a small change in its direction at the output of the prism. In the same way, only large shifts in the wavelength of the beam will result in noticible changes in the beam’s direction at the output of the prism. By introducing other materials into the prism and forming systematic arrangements of these materials in what are known as photonic crystals, we can create large changes in the beam’s direction. Creating a photonic crystal by stacking alternating layers of material, by creating checkerboard lattices of material, or by introducing any other type of periodic variation in material allows us to create larger prism effects known as “superprism” effects.

A superprism is an optical device similar to a conventional prism only with two enhanced properties: (1) *super-dispersion* and (2) *ultra-refraction.* Just as a conventional prism separates light into multiple wavelengths, a superprism separates these wavelengths over wider angles (Figure 1.1). We will term this property "super-dispersion." A superprism can also be used to magnify the angle of propagation of a single wavelength beam (Figure 1.2) to steer the beam over wider angles. We will term this second property "ultra-refraction."

FIGURE 1.1 Illustration of the "super-dispersion" property of a superprism versus dispersion in a conventional prism. For a smaller range of wavelengths, the dispersion in a superprism is much stronger [1].

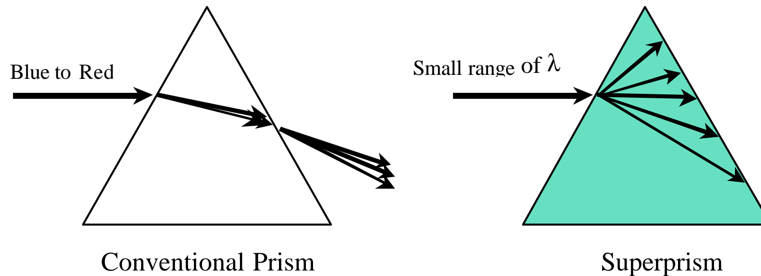

Being able to realize these enhanced effects of a superprism would be very useful for a number of applications ranging from enhanced devices for wavelength division multiplexed (WDM) systems to a new class of ultra-refractive optical elements for beam

manipulation [2]. An additional advantage of the superprism is that it can reduce the size of many of these optical systems [3]. Large spectral separation and bending of incident light can be more compactly controlled using one small superprism rather than a larger system composed of multiple prisms, lenses, and mirrors.

FIGURE 1.2 Illustration of ultra-refraction in a superprism. A small swing in the incident angle results in a large swing in the output angle.

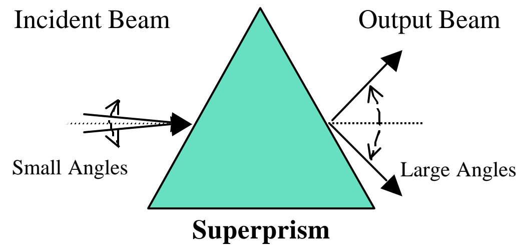

A number of groups have previously designed and fabricated photonic crystal devices for the purpose of observing superprism effects. *Kosaka, et al.* used a three-dimensional photonic crystal to demonstrate super-dispersion and ultra-refraction [1], [2]. The device was fabricated as a 3D hexagonal lattice using self-assembling silicon and silicon oxide layers. For a wavelength difference of 0.01μm, they demonstrated a 50 degree difference in the beam's direction of propagation within the device. In a conventional silicon prism, this shift would be less than one degree. They also demonstrated that changing the incident angle from +/-7 degrees at the input results in a swing of +/- 70 degree within the crystal. Though these results seem promising as a demonstration of superprism phenomena in photonic crystals, such a three dimensional structure is complicated to fabricate. In addition, the Kosaka experiment does not report on the angular characteristics of the beam once it exits the photonic crystal. This is probably due to the fact that once the beam exits the crystal, the superprism effect will reverse itself as the beam "refracts back" at the output of the device.

In order to circumvent the fabrication complexities associated with the 3D superprism while preserving the superprism effect at the output, *Nelson, et al.* demonstrated that strong wavelength dispersion effects can be achieved using a simpler one dimensional photonic crystal [3]. Nelson introduces a wavelength dependence into the angle of propagation by using the dispersion properties of a dielectric stack. As a beam propagates within the dielectric stack, the dispersion between wavelengths translates into a lateral shift in the position of the beam upon exiting the crystal. The dispersive effect is maintained as the beam exits the device. While the fabrication of this 1D structure is indeed simpler, this device shifts the location of the output beam rather than affecting its angle of propagation. In addition, the multiple reflections within the dielectric stack introduce heavy losses into the system.

We believe that the superprism effects of super-dispersion and angular magnification can be achieved using 2D photonic crystals. By using a 2D structure, we can keep the fabrication complexity relatively simple, while creating effects that are angular in nature. In addition, our device design proposes a way in which these superprism effects can be observed not only within the crystal, but at the output as well.

2.0 DESIGN THEORY & SIMULATION

2.1 How can we make a prism "super"?

The prism effect in a conventional prism is due to different frequencies refracting at different angles within a material according to Snell's Law. We can illustrate this fundamental effect using *dispersion surfaces* as shown in Figure 2.3.

FIGURE 2.3 (a) The dispersion surface of an arbitrary isotropic medium showing the direction of the **k**-vector and the direction of power propagation [4]. (b.) The dispersion surfaces for multiple frequencies in an isotropic medium. Each frequency has a dispersion surface of a different radius.

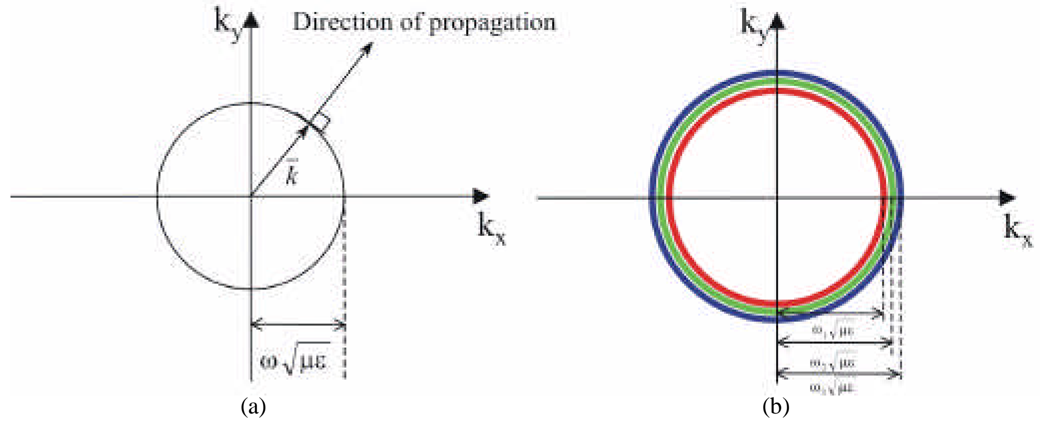

A *dispersion surface* maps out the angular dependence of the wave vector **k** for the propagation of light within a particular medium. For instance, in a medium of uniform refractive index (an isotropic medium) the dispersion surface is a circle. That is, for a given frequency, the magnitude of the wave vector remains constant for every direction of propagation in the material. The dispersion relation determines the length of the wave vector according to:

$$k = \omega\sqrt{\mu\varepsilon} \quad \textbf{(EQ 2.1)}$$

Therefore for each frequency, the radius of the dispersion surface will be different due to the change in ω and ε. The wave vector will propagate in the direction normal to the dispersion surface according to the group velocity:

$$\vec{v}_g = \vec{\nabla}_k\omega \quad \textbf{(EQ 2.2)}$$

In an anisotropic medium, as shown in Figure 2.4, the dielectric constant is no longer uniform in all directions implying that the dispersion surface is no longer a circle. In a uniaxial medium, for example, the dielectric constant along one principal axis, the optic axis, is different from the dielectric constant along the other two axes. For this type of medium, the component of the wave polarized along the optic axis (extraordinary wave), has an

elliptical dispersion surface. The component polarized along one of the other two axes (ordinary wave), has a circular dispersion surface. A uniaxial medium therefore illustrates two properties of interest: (1) the magnitude of the **k**-vector depends on its orientation and (2) the direction the wave vector propagates also depends on orientation.

FIGURE 2.4 The dispersion surfaces of a uniaxial medium showing the difference in the direction of the **k**-vector versus the direction of power propagation for the extraordinary wave [4].

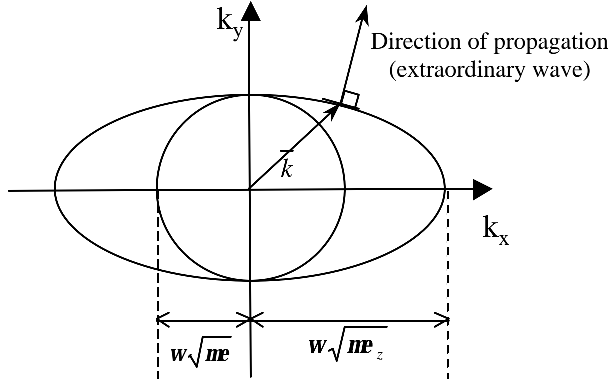

If we send light across a boundary between one medium and another, the **k**-vector moves from one dispersion surface to another as shown in Figure 2.5. In the process, the boundary conditions on the electric and magnetic fields must be satisfied. If a wave is travelling from air to a material with a higher index of refraction such as glass, the k-vector moves from a dispersion surface with a smaller radius, to a dispersion surface with a larger radius. According to Maxwell's equations, the tangential components of the electric and magnetic fields must remain constant across the boundary so that:

$$k_{x,\,air} = k_{x,\,glass} \qquad \textbf{(EQ 2.3)}$$

As a result, the normal component of the k-vector will change in magnitude and the wave vector has refracted into the new medium changing its direction.

FIGURE 2.5 The dispersion surfaces on each side of a boundary between air and a higher index material.

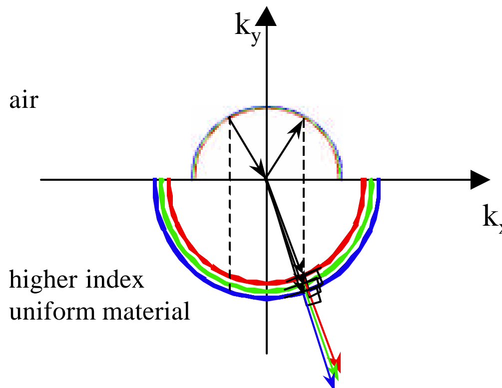

We can now use this model of dispersion surfaces to identify the effects we are looking for in a superprism: large angular magnification, and the super-dispersion of frequencies. In order to observe large angular magnification and super-dispersion, we need to find a material in which the properties of the **k**-vector are highly sensitive to changes in direction; *i.e.* a material that is highly anisotropic.

Consider, for example, a material with a dispersion surface such as the one shown in Figure 2.6.

FIGURE 2.6 Superprism effects using large changes in the group velocity. (a) Illustration of angular magnification at a constant frequency in a superprism. (b) Illustration of super-dispersion in the superprism.

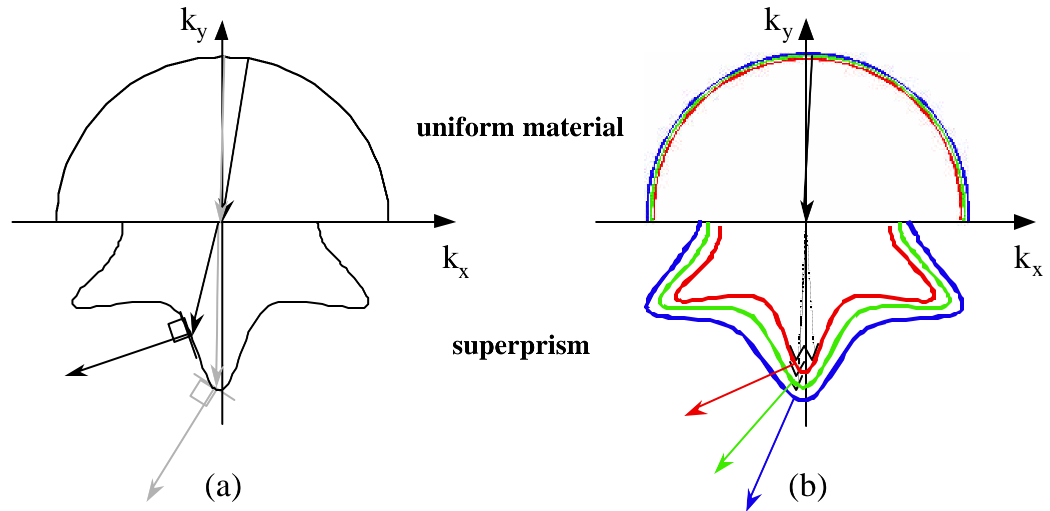

The sharp bends in the dispersion surface allow us to create highly dispersive effects using variations in the group velocity. The group velocity depends on the slope of the dispersion surface. For orientations of the **k**-vector in the direction of the sharp bend, the group velocity is highly sensitive to changes in direction. As shown in Figure 2.6(a), at small angles, a small change in the incident angle (shown with the black and gray arrows) will result in a large change in the group velocity--the direction of propagation of the **k**-vector. The phase matching condition on the tangential **k**-vector is met as the wave crosses the boundary.

Figure 2.6(b) illustrates super-dispersion using a material with the same dispersion surface as in Figure 2.6(a). As stated previously, the radius of the dispersion surface changes with frequency. Thus the super-dispersion of different frequencies is due to the fact that for a given **k**-vector, the difference in the group velocity for each frequency is very large, *i.e*. the slope of the dispersion surface changes very rapidly with frequency. Note that the dispersion surfaces corresponding to different frequencies in the uniform material are much closer together than the dispersion surfaces in the superprism. This result enhances the super-dispersion effect.

We can also create highly dispersive effects by using changes in the phase velocity as shown in Figure 2.7.

FIGURE 2.7 Highly dispersive effects using differences in phase velocity.

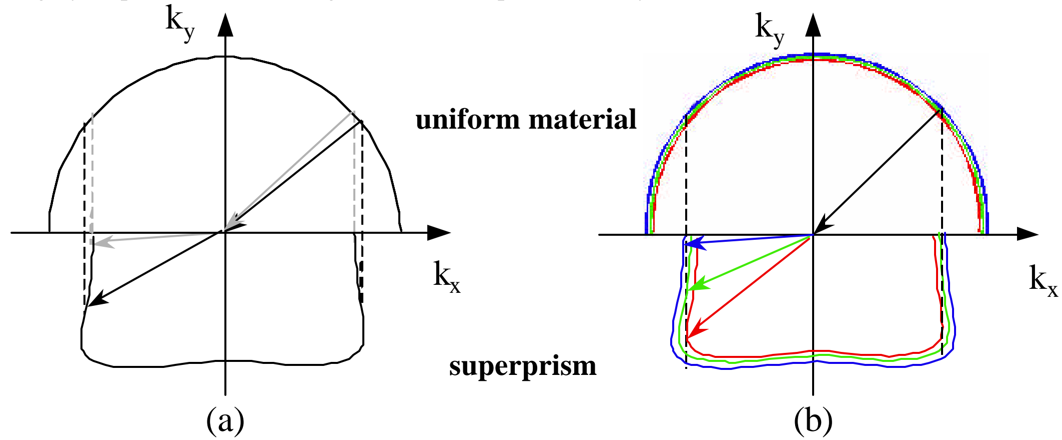

The phase velocity equals the magnitude of the **k**-vector. The phase matching condition on the tangential **k**-vector is shown with the dotted lines. The flatness of this dispersion surface allows small variations in the input angle to translate into large variations in the magnitude of the k-vector as shown in Figure 2.7(a). Figure 2.7(b) shows how this flatness allows us to realize the super-dispersion of frequencies by using large changes in the phase velocity. In Section 2.3 we will show how we use the phase velocity to demonstrate superprism effects that can be observed in air.

2.2 What are Photonic Crystals?

We can not observe large angular magnification and super-dispersion using uniform materials because their dispersion surfaces show little spatial or spectral variation. For our superprism, we are looking for a highly anisotropic medium where properties of the **k**-vector are very sensitive to changes in direction and frequency. A new class of structures, called photonic crystals, provide us with the properties we are looking for.

Photonic crystals are artificial structures composed of a periodic variation in the index of refraction. For example, this periodic variation may be fabricated in one dimension using an alternating stack of high and low index materials, in two dimensions as spatially periodic dielectric rods, or in three dimensions as a spatially periodic lattice (Figure 2.8). Introducing a spatial variation in the index of refraction of the material introduces a number of interesting properties that can be used to control and manipulate light as it passes through the crystal.

As light passes through any periodic structure, it scatters at each dielectric boundary. A dielectric mirror is one example of a 1D periodic structure which may use this scattering to

reflect light of a particular frequency. The mirror is composed of a stack of alternating layers of dielectric material (as in Figure 2.8(a)) so that scattered waves at this frequency will destructively interfere with the incident waves. Light at this frequency cannot pass through the material and is reflected. At the same time, other frequencies passing through the material will constructively interfere upon scattering and are transmitted rather than reflected.

FIGURE 2.8 From left to right, examples of (a) one, (b) two, and (c) three dimensional photonic crystals. The different colors represent materials of different dielectric constants [5].

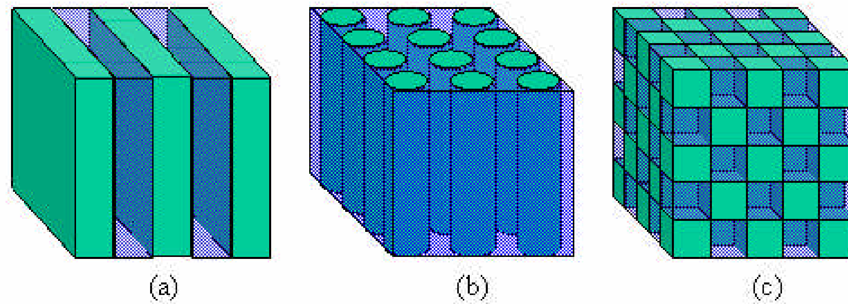

FIGURE 2.9 Sketches of photonic band structures for propagation perpendicular to the plane of a 1D photonic crystal made of stacked dielectric slabs as in Figure 2.8(a). (a) Band structure with slabs having the same index of refraction. (b) Band structure with slabs alternating between high and low refractive index materials. The high index contrast creates a band gap in allowed frequencies for this case [5].

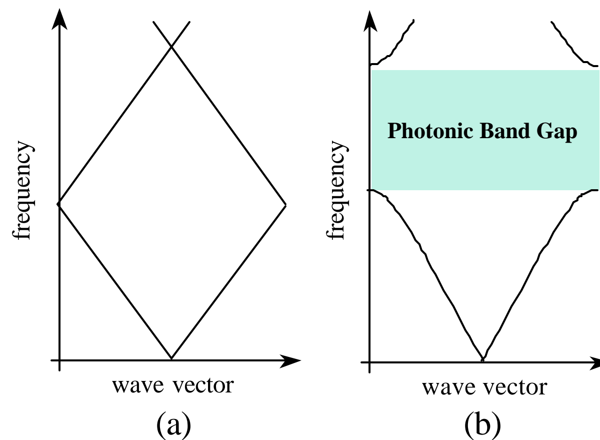

The behavior of light as it passes through a photonic crystal can be described by a photonic band structure as shown in Figure 2.9. The photonic band structure describes the relationship between the frequency and the wave vector for light traveling normal to the plane of the slab. The band structure for the 1D photonic crystal with layers of high index contrast (Figure 2.9(b)) exhibits a “gap” of frequencies for which no light may propagate through the material. The crystal with no index contrast (Figure 2.9(a)) has no such gap. The frequencies that lie in this photonic band gap are frequencies that are reflected in the case of the dielectric mirror.

The photonic band structure also illustrates some other useful properties. The phase velocity at each frequency can be calculated using:

$$v_p = \frac{\omega}{k} \quad \textbf{(EQ 2.4)}$$

The group velocity can be calculated from the slope of the band structure using:

$$v_g = \frac{d\omega}{dk} \quad \textbf{(EQ 2.5)}$$

The dispersion in frequencies is then related to the derivative of the group velocity. Looking at the band structure, we can see that the group velocity (slope) changes very rapidly at the edges of the band gap implying a frequency range of high dispersion. This dispersion only occurs for the component of a plane wave incident normal to the slab. Any component of propagation parallel to the slab boundary does not experience scattering because there is no periodicity in this direction. Therefore, for angles of incidence other than normal, there are no photonic band gaps. As a result, the angular dispersion is less severe.

If we create a periodicity in two or three dimensions, we can create a photonic crystal with a band gap for incident light in multiple directions. In two and three dimensions, the periodicity of the crystal can take on a number of forms. For example, a two dimensional photonic crystal can be created using rods of dielectric material suspended in a different bulk dielectric material (as in Figure 2.8(b)). These rods may be arranged periodically in multiple ways (*e.g.* a square lattice or a hexagonal lattice). The rods may be of a higher dielectric constant than the bulk, or vice versa. In three dimensions, the periodicity can be created in even more ways with different shapes and lattice configurations.

The configuration of each photonic crystal determines the characteristic shape of its band structure. The wave vector orientations with highest dispersion in the band structure will be centered along lines of periodicity in the structure. For the 1D slab photonic crystal (PC), there was only one such direction--the direction normal to the slab surface. In the 2D PC, the periodicity created by the lattice of columns creates two unique directions of periodicity. Creating multiple dimensions in the periodicity allows us more flexibility in determining the directional as well as spectral characteristics of the band structure.

Since the band structure only plots the frequency vs. wave vector relationship for directions along the lines of periodicity, we cannot map the whole dispersion surface of a photonic crystal using one band structure alone. We construct the full dispersion surface for each mode of propagation by plotting the magnitude of the **k**-vector for all possible orientations at a constant frequency. By traveling along a line of constant frequency on the band structure, we intersect points on the dispersion surface corresponding to the directions of periodicity in the photonic crystal. This idea will become more apparent in the next section as we present the band structure and dispersion surface for our superprism photonic crystal.

2.3 Superprism Design and Simulation

The superprism device designed and fabricated in this thesis consists of a 2D photonic crystal with a square lattice of air holes in gallium arsenide (GaAs). Our initial design has focussed on realizing angular magnification such that a small continuous angular sweep of the beam at the input will be amplified at the output of the device. Our goal has been to design the device in order to observe angular magnification at the output of the device in air. Previous experiments have not demonstrated angular dispersion in air but have only observed the phenomenon within the photonic crystal [1].

The top view of the design shown in Figure 2.10 shows how the GaAs region is shaped as a parallelogram with the photonic crystal occupying a square region within the parallelogram. The orientation of the parallelogram with respect to the photonic crystal edge is designed such that light entering the input facet at near normal incidence then exits the output facet at larger angles centered around the normal direction. The ideal performance is designed such that an input angular sweep of approximately +/-2° will be amplified to about +/-30° at the output for a wavelength of 3.1 µm. A thick aluminum oxide (Al_xO_y) layer is used to minimize radiation loss into the GaAs substrate. The depth of the holes and the parallelogram sidewalls will be as deep as possible to facilitate coupling from an input fiber.

FIGURE 2.10 Superprism device schematic (not to scale).

Top View:

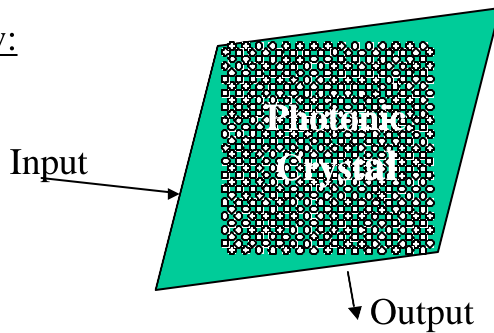

- a square lattice of air holes
- holes occupy a square region in GaAs
- lattice is rotated 45deg with respect to square region
- square region is aligned within a parallelogram mesa

Cross Section:

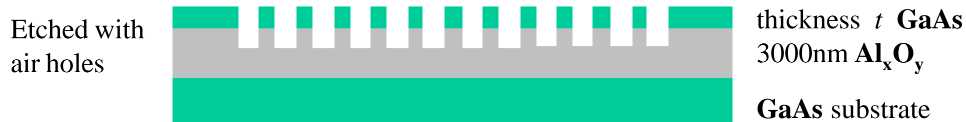

Design: λ=2800 to 3800 nm;
PBG Lattice Constant: a=λ*0.24
GaAs Thickness t= λ*0.144
Hole Radius= λ*0.096

For **l** *=3125* nm*:*
a=750nm
t=450nm
r=300nm

To proceed with the design of our superprism, we calculated dispersion surfaces for several modes within a 2D photonic crystal consisting of air columns in GaAs. As discussed earlier in this chapter, the direction of wave propagation inside the photonic crystal is given by the direction of the group velocity (*i.e.* the direction normal to the dispersion surface). However, the direction of propagation as the beam exits the crystal is determined by the phase velocity due to the phase matching condition on the k-vector at the boundary. Therefore, for a photonic crystal superprism to have ultra-refractive effects that are preserved at the output of the device, we must utilize regions of the dispersion surface that have highly sensitive phase velocity behavior. This is the key difference between our work and previous work thus far.

For the dielectric configuration shown in Figure 2.10, we have calculated the relevant dispersion surface shown in Figure 2.11. The results are presented on a normalized basis. The computation assumes a finite slab thickness of 0.6a and a hole size of 0.4a. The indices of refraction used were 3.4 and 1.5 for the GaAs and aluminum oxide layers respectively. This calculation is for guided modes with the magnetic field concentrated in the perpendicular polarization. The computed dispersion surface has a fairly flat region which is ideal for ultra-refraction.

FIGURE 2.11 Dispersion surface calculation for photonic crystal design. The square lattice orientation is shown in the inset [7].

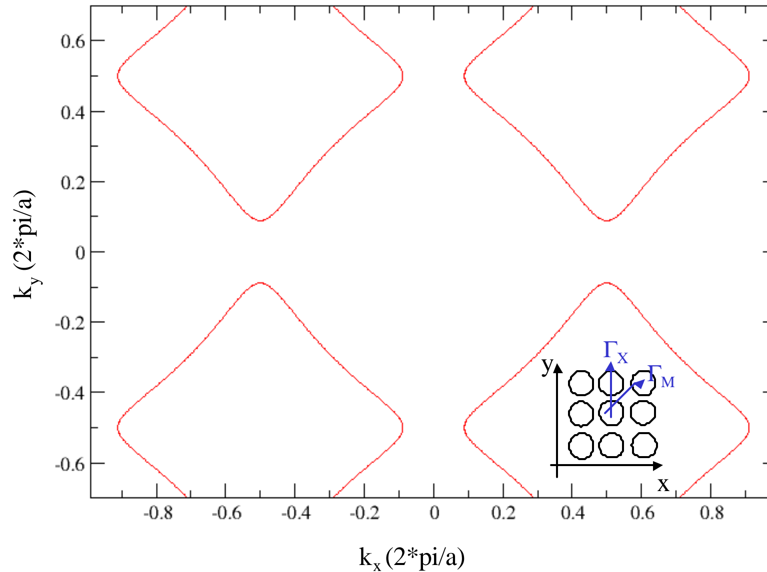

The method used to compute the dispersion surface in Figure 2.11 was as follows. The dispersion relation for guided modes propagating in a planar slab was computed using preconditioned conjugate gradient minimization of the Rayleigh quotient in a plane wave basis [6]. A numeric root-finder was used to solve for the exact wave vectors that correspond to a particular frequency. This computation was carried out for every orientation throughout the entire Brillouin Zone to map out the dispersion surface.

FIGURE 2.12 The band structure for the superprism photonic crystal [7].

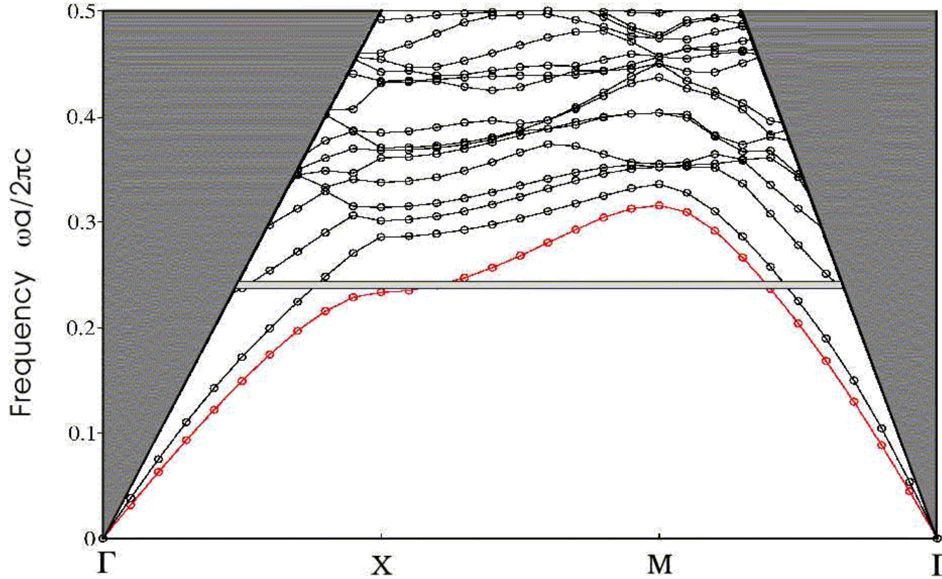

FIGURE 2.13 Explanation of Superprism ultra-refraction using the dispersion surfaces in the photonic crystal and GaAs [7].

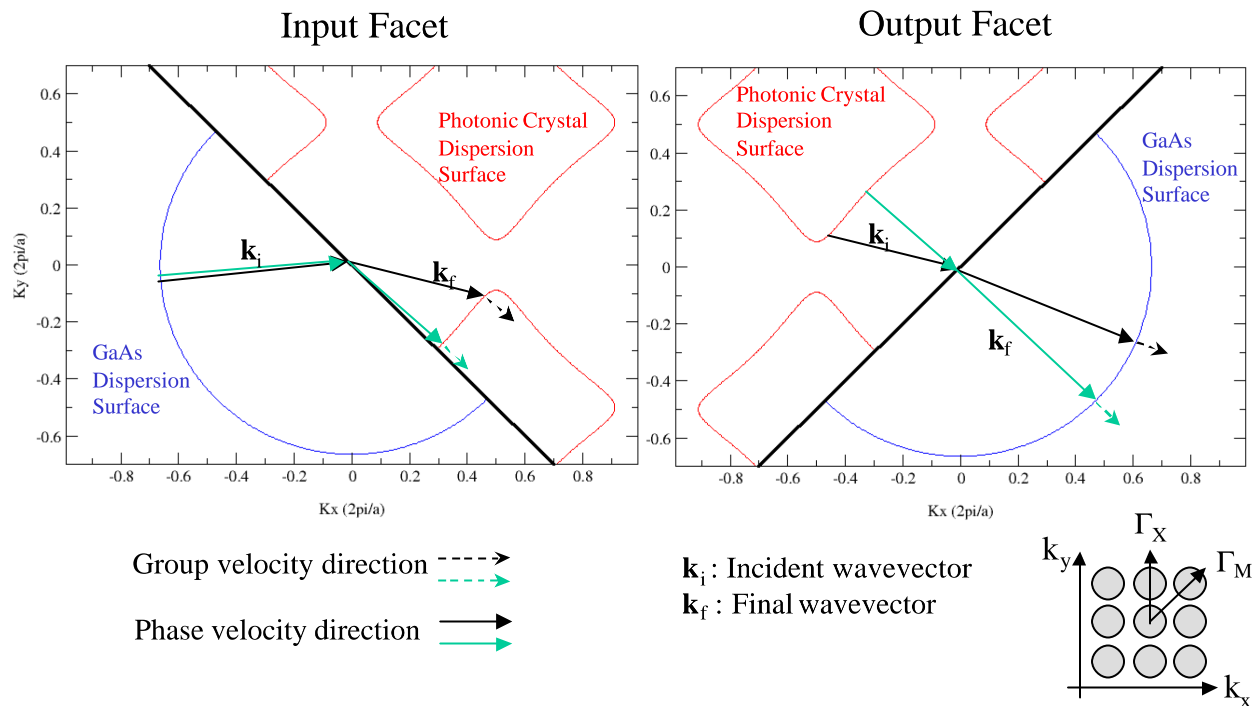

Figure 2.12 is the band structure for the superprism's photonic crystal. The computation uses the same assumptions as the dispersion surface calculation in Figure 2.11. The horizontal line represents an equi-frequency line at the normalized design frequency of 0.24.

Our device operates by coupling to the lowest mode shown in this band structure. As stated earlier, we have assumed an input beam polarized such that the magnetic field is concentrated in the z direction. The lowest order mode corresponds to this polarization and is therefore the only mode that the input beam will couple to. Though the equi-frequency line intersects other higher modes, these modes correspond to other polarizations with the electric field concentrated in the z direction. In addition, the orientation of our photonic crystal is such that the beam is incident upon the GaAs/photonic crystal boundary at an angle and will only couple to the lowest order mode independent of polarization. This result is more clearly illustrated in Figure 2.13.

The ultra-refraction property of our superprism is illustrated in Figure 2.13. The boundary between the gallium arsenide and the photonic crystal lies along the Γ-M symmetry line of the square lattice. The two different arrows in Figure 2.13 represent **k**-vectors for two different input beams which differ by only a small angle. As the beam propagates from GaAs into the photonic crystal, the phase matching condition on the tangential component of the **k**-vector must be met. The beam refracts into the photonic crystal as the **k**-vector moves from the GaAs dispersion surface to the photonic crystal dispersion surface.

The small difference between the two input wave vectors translates into a large change in the phase velocity inside the photonic crystal due to the flatness of the dispersion surface. As the two beams exit the photonic crystal at the output facet, the phase matching condition is met again and the angle between the wave vectors is greatly magnified.

Figure 2.13 does not show the beams as they propagate from air to GaAs at the input and from GaAs to air at the output. However, the angular difference between the two beams will only be enhanced as the beams propagate into air. The result is a large angular sweep at the output for a very small angular sweep at the input. Similar considerations can also be used to realize frequency super-dispersion using a broadband source at a fixed angle of incidence.

The photonic crystal dispersion surfaces shown in Figure 2.11 and Figure 2.13 correspond to the lowest order mode shown in the band structure in Figure 2.12. By traveling along a line of constant frequency on the band structure, we intersect points on the dispersion surface corresponding to **k**-vectors in the directions of periodicity in the photonic crystal, which are the Γ-M and Γ-X directions for a square lattice. If there are multiple modes at a particular frequency, there are multiple dispersion surfaces.

Traveling along the equi-frequency line in Figure 2.12, we intersect both the lowest order mode, and two higher order modes. These two higher order modes have dispersion surfaces shaped like circles with smaller radii. For near normal incidence, an input beam may be able to couple to these modes-though the coupling may be weak due to differences in polarization. However, we have designed the input facets such that the beam is incident

upon the photonic crystal at steep angles as shown in Figure 2.13. At steep angles of incidence, the input **k**-vector will not be able to couple to these higher order modes because the phase matching condition cannot be met. Therefore, our beam will only couple to the lowest order mode in the band structure enabling us to concentrate more power in the mode of interest for our superprism.

FIGURE 2.14 Time domain simulation of superprism ultra-refraction. The simulation was performed on a simplified 2D structure which did not consider the effects of a finite device thickness [7].

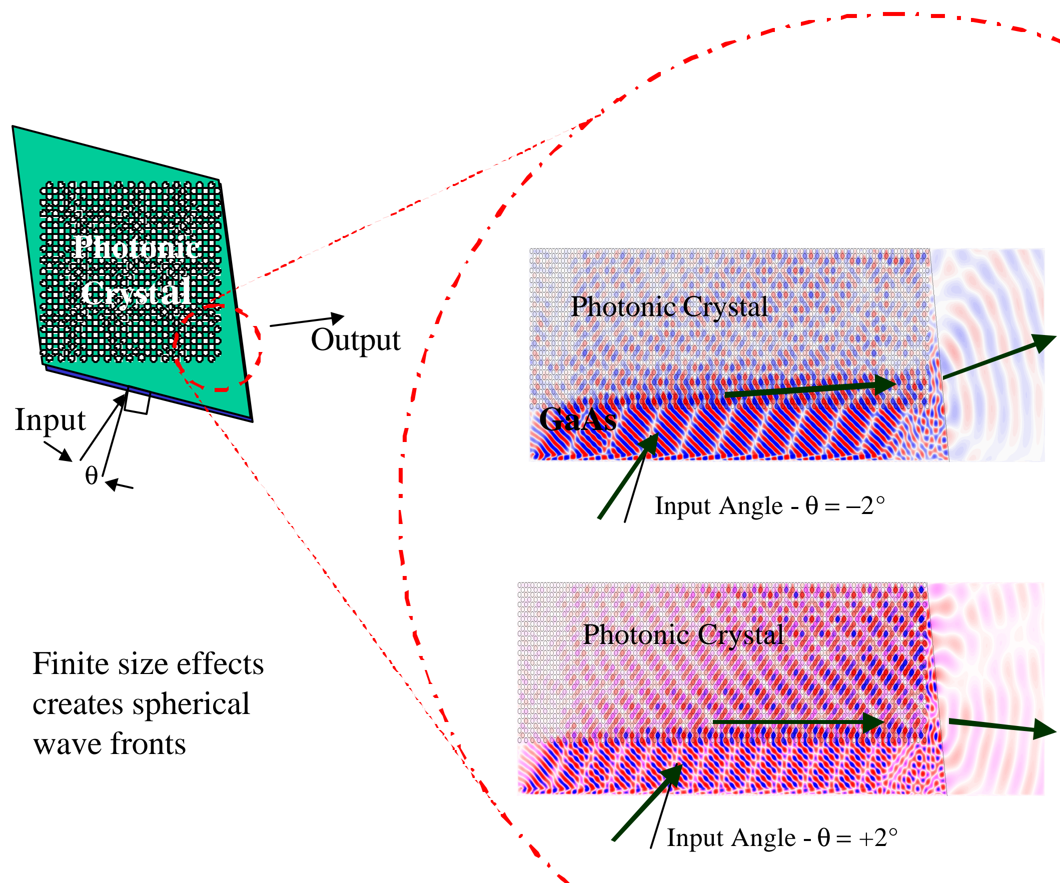

To demonstrate the experimental feasibility of our ideas we have carried out finite-difference time-domain simulations on a simplified system. The simplified system has the same photonic crystal lattice structure as our device but is purely 2D (assumes infinite structure thickness) and is reduced in size. In the simulation, shown in Figure 2.14, a plane wave generated by a straight line of dipoles is launched into the GaAs region and propagates into the photonic crystal. The figures show snapshots of the z component of the magnetic field distribution.

Two Bloch waves are excited within the crystal. As they propagate, they are severely refracted. Upon exiting the photonic crystal, one of the Bloch waves is internally reflected

at the GaAs/Air interface allowing a single Bloch wave to couple out into air. As the incoming beam is changed by +/-2°, the output beam sweeps through a large angular range of +/-30°. In the high dielectric GaAs region, a fringe pattern can be observed due to interference between the incident and reflected beams. The finite size of the simulation also causes the output beam to appear spherical. The arrows within the figures are just to guide the eye but demonstrate how the direction of the beam shifts with the slight change in the input angle.

3.0 RESEARCH APPROACH

3.1 Research Objective

Our goal is to design and fabricate a superprism device using a two dimensional photonic crystal in a gallium arsenide material system. The device will allow a small angular sweep at the input to translate into a large angular sweep at the output (i.e. ultra-refraction). In addition, an input beam with a small spread in frequencies will result in a large angular separation of these frequencies at the output (super-dispersion).

The superprism is composed of a two dimensional photonic crystal with a square lattice of air holes in gallium arsenide (see Figure 2.10). The photonic crystal rests on a thick layer of aluminum oxide on a gallium arsenide substrate. The depth of the air holes is as deep as possible. The feature sizes of the photonic crystal are scalable depending on the wavelength of operation. Our desired wavelength range of 2.8 to 3.8 μm implies a lattice constant of 672 to 912 nm, and a hole radius varying between 269 and 365 nm. The input and output facets are air-GaAs boundaries positioned at specific design angles with respect to the photonic crystal. The total thickness of the device (excluding substrate) is about 3.5 μm while the top surface will have an area of about 2 cm x 2 cm.

The orientation of the parallelogram with respect to the photonic crystal edge is designed such that light entering the input facet at near normal incidence, then exits the output facet at magnified angles centered around the normal direction. The ideal performance is designed such that an input angular sweep of approximately +/- 2° will be amplified to about +/- 30° at the output for a wavelength of 3.1 μm.

3.2 Design Tolerances

In order to identify the steps necessary to fabricate the superprism, we needed to determine a number of tolerances on the device design. The results are presented in Figure 3.1.

Changing the ratio of hole size to lattice constant (*r/a*) changes the frequency at which the dispersion surface is flat thereby shifting the frequency at which we will observe our performance specifications. By simulating a change in *r/a* from 0.40 to 0.35 and recalculating the dispersion surface, we found that the frequency at which the dispersion surface was now flat (the performance frequency) decreased by about 7%. An error in *r/a* by -0.05 would shift our performance frequency from 3.1 μm to 2.9 μm which is acceptable from a testing perspective. We therefore aim to stay within this error of 7% or r = 300 nm +/- 38 nm. However, since the hole size is susceptible to a number of sources of variation from the lithography as well as etching steps, this parameter is anticipated to be the most difficult parameter to meet.

Lattice squareness refers to the degree to which the grid of holes in the photonic crystal is actually square. Errors in the squareness of the grid may be introduced in the fabrication

process due to the need for two exposures when patterning holes using interference lithography. Small errors of this type would again alter the frequency at which the dispersion surface is flat because the periodicity in hole spacing would be altered. By simulating an error of 10º in the distortion of the square grid, we found that the performance frequency increased by about 7% from 3.1 µm to 3.3 µm. To keep the error below 1%, we aim for a tolerance of +/-1°. Please see Section 4.3 for a discussion of how this tolerance is met.

FIGURE 3.1 Superprism device tolerances

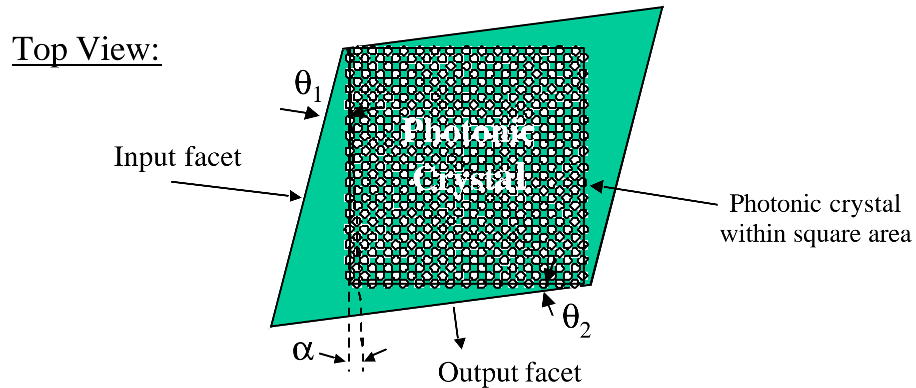

1) **radius of holes:** r = (0.40 +/- 0.05)*a where a is the lattice constant => r=300+/-38 nm

2) **lattice squareness:** the angle between two lattice vectors = 90 +/- 1º

3) **alignment of square shape to parallelogram:** θ_1=38 +/- 1º, θ_2=11+/- 1º

4) **alignment of lattice edge to square edge:** the angle α between a line of holes and the square edge α = 0.0 +/- 0.5º

As stated above, the angled facets of the device allow light entering the input facet at near normal incidence to then exit the output facet at larger angles centered around its normal direction. Small errors in these angled facets with respect to the boundary of the photonic crystal would shift the input/output wavevector angles to directions which are not centered about the normal. This error would not otherwise effect the performance of the device. We therefore aim for a tolerance of +/- 1º on this specification.

The use of interference lithography to pattern the large area of photonic crystal holes may introduce errors in the alignment of the hole lattice to the edge of the square region. Ideally, the edge of the square area should be completely parallel to a line of holes of the photonic crystal so that α = 0º (as shown in Figure 3.1). A non-zero α will rotate the dispersion surface with respect to the GaAs-photonic crystal boundary. We have designed the device such that a +/- 2º input swing will result in an output swing of +/- 30º. Errors which rotate the dispersion surface would change this input/output angular magnification performance because we would be utilizing a different part of the dispersion surface. Through simulations, we have estimated that an α = 1º error in boundary alignment would

change our design performance in two ways depending on whether α is positive or negative: a +/- 1.5° input translating to +/- 30° output, or +/- 2.5° input translating to +/- 30° output. We therefore set our tolerance on this alignment specification to $\alpha = 0$ +/- 0.5°.

3.3 Fabrication Sequence

The following is a general outline of the steps necessary for the successful fabrication of the GaAs superprism considering the tolerances discussed in Section 3.2. Please refer to Chapter 4 for detailed discussion and results relating to each of the fabrication steps.

FIGURE 3.2 Growth of epilayer, sputtering of SiO_2 and Cr evaporation

- Growth of device epilayer using molecular beam epitaxy: 450nm **GaAs**, 3000nm **AlAs** on **GaAs** substrate

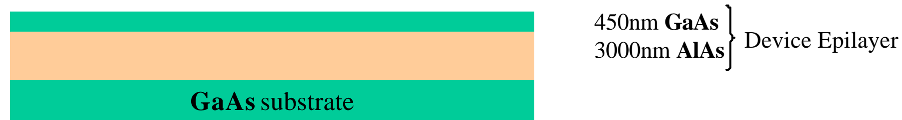

- Substrate coated with 300nm SiO_2, 50nm chrome

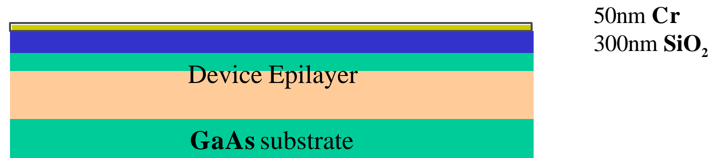

The device epilayer which consists of 450 nm GaAs and 3000 nm AlAs on a GaAs substrate is grown using molecular beam epitaxy. A 300 nm layer of SiO_2 is sputtered using the sputtering system in the Nanostructures Laboratory (NSL). This SiO_2 layer will be used as a hard mask for etching the GaAs/AlAs epilayer. A 50 nm chrome layer is deposited using an evaporator. This layer will be used to define the parallelogram and square shape of the device.

Figure 3.3 is a general schematic of the photolithography mask patterns used to define the device shape. Please see Chapter 4 for more detailed discussion. Two photolithography steps will be used: the first using Mask 1 will allow for the exposure of holes within the square area of the device, and the second step using Mask 2 will protect the square area as the unwanted holes outside the parallelogram are etched away. An alignment grid on Mask 1 aids in the alignment of the holes to the device shape. Alignment crosses on Mask 1 and alignment dots on Mask 2 aid in the alignment of the two patterns to each other.

FIGURE 3.3 Photolithography mask design schematic. Mask 1 and Mask 2 are two 4" masks with the chrome pattern on glass (mask outline not shown).

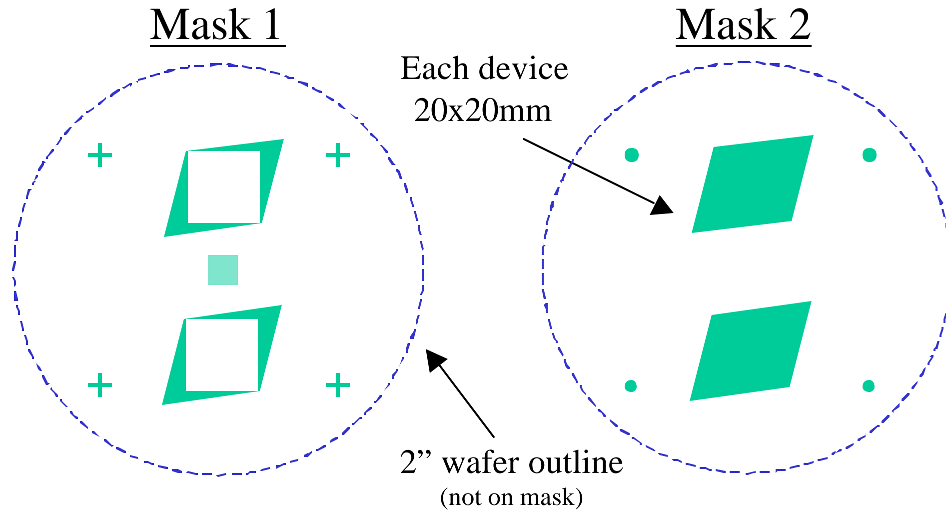

FIGURE 3.4 Photolithography with Mask 1

• use Mask 1 to expose/develop square and parallelogram in photoresist with alignment marks and alignment gratings

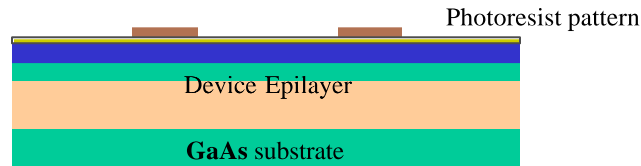

• Wet etch chrome (CR7 etchant); acetone/ash photoresist

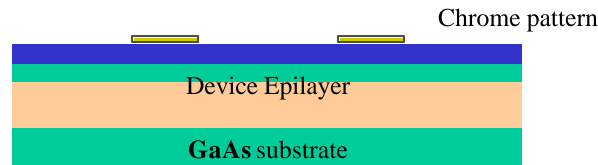

Pattern on wafer:

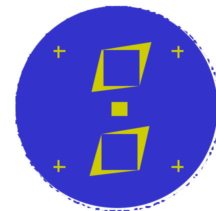

The first photolithography mask is used to contact expose the parallelogram and square shapes in photoresist as shown in Figure 3.4. This mask exposes cross-shaped alignment marks which are used to align this pattern to the pattern later exposed using Mask 2. The square area in the middle of the wafer is a grid which is used to align the Interference

Lithography exposure to this Mask 1 pattern. A wet etch is used to transfer the resist pattern to the chrome layer.

FIGURE 3.5 Interference Lithography with use of trilayer resist stack. Please see Chapter 4 for a discussion of thicknesses.

- Spin trilayer: thick Anti-reflective coating (ARC), thick SiO_2 interlayer, photoresist

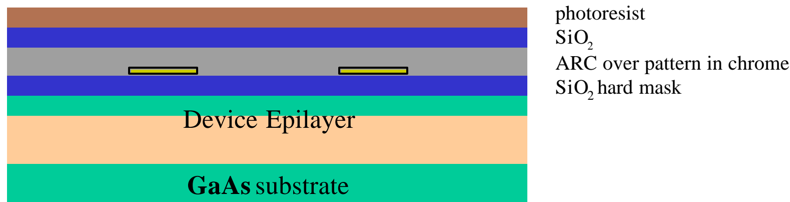

- Expose/develop holes in photoresist using interference lithography (IL)
  - use mask 1 grid to align hole pattern to device shape

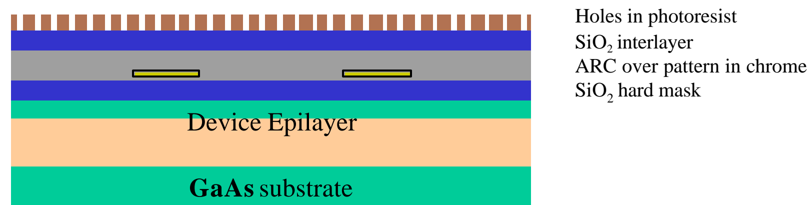

Figure 3.5 shows the preparation of the substrate and the subsequent Interference Lithography exposure. Interference lithography is used to pattern the whole wafer with holes. The trilayer resist stack consisting of: photoresist, SiO_2 interlayer, and anti-reflective coating (ARC) is used to minimize reflections off the substrate during the exposure and facilitate pattern transfer to the SiO_2 hard mask layer. Please see Chapter 4 for a discussion of the relevant thicknesses. The alignment grid on the wafer is used to align the hole pattern to the device shape in chrome.

Figure 3.6 shows the transfer of the hole pattern to the SiO_2 hard mask layer using Reactive Ion Etching (RIE). The gases used to etch the SiO_2 and ARC layers are CHF_3, and He/O_2 respectively. A CHF_3 RIE step is then used to transfer the pattern into the SiO_2 hard mask layer. The chrome layer will prevent the etching of holes outside the square area within the parallelogram shape as shown by the pattern on the wafer in Figure 3.6. A He/O_2 ash step is used to remove any remaining ARC.

FIGURE 3.6 Reactive Ion Etching of trilayer resist stack and SiO_2 hard mask. The deep holes shown are only to illustrate pattern transfer through each layer. As the hole pattern is transferred through each layer, layer thicknesses decrease due to sputtering and etching thus avoiding unnecessary high aspect ratio etching.

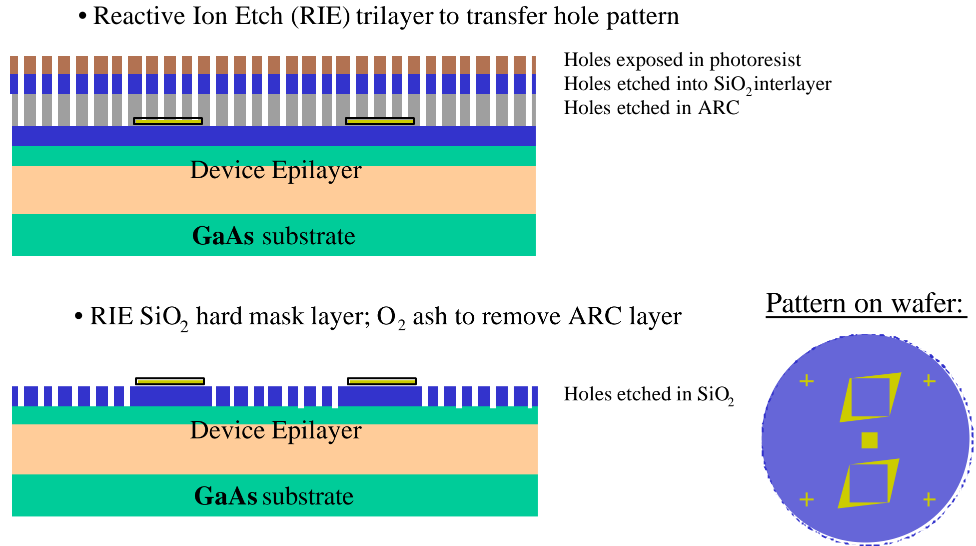

FIGURE 3.7 Photolithography using Mask 2

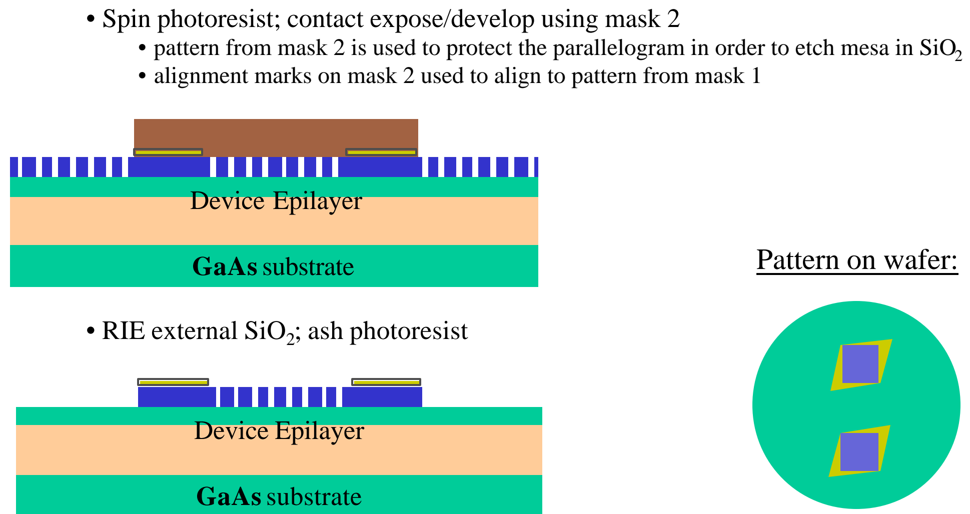

The second photolithography step shown in Figure 3.7 uses Mask 2 to expose the device parallelogram shape with a closed square area to protect the holes inside. Alignment marks are used to align Mask 2 to the pattern from Mask 1. An RIE step is then used to etch away the holes in the SiO_2 hard mask outside of the parallelogram area.

FIGURE 3.8 Reactive ion etch substrate and oxidize AlAs layer

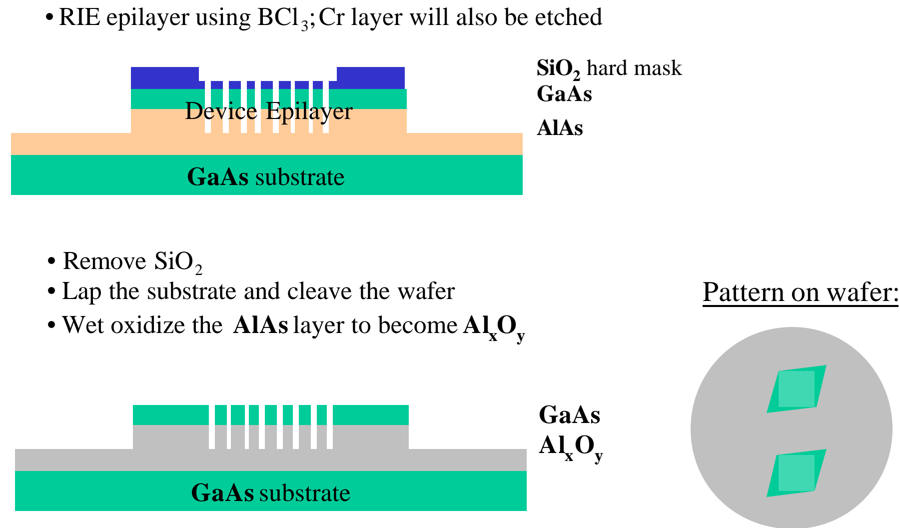

A final RIE step using BCl_3 shown in Figure 3.8 transfers the hole pattern and the device shape into the GaAs/AlAs epilayer. Any remaining SiO_2 is removed using CHF_3 RIE. The substrate is thinned through lapping and we then cleave the wafer to separate the individual devices. The last step is a wet oxidation of the AlAs layer creating our low index Al_xO_y layer.

All fabrication steps are performed in laboratories at the Massachusetts Institute of Technology. The GaAs/AlAs epilayer is grown in the Chemical Beam Epitaxy Laboratory, most processing, including lithography and reactive ion etching, is performed in the Nanostructures Laboratory, and the die sawing is performed in the Microsystems Technology Laboratory.

Testing of the device will be performed in collaboration with Rockwell Science Corp.

4.0 DISCUSSION & RESULTS

4.1 Molecular Beam Epitaxy Results

The GaAs heterostructure shown in Figure 4.1 was grown using the Riber Instruments gas source molecular beam epitaxy (GSMBE) system in the Chemical Beam Epitaxy group at MIT. The structure was grown successfully with the following layers:

- 400 nm GaAs
- 50 nm $Al_{0.50}Ga_{0.50}As$
- 3000 nm AlAs
- 50 nm $Al_{0.50}Ga_{0.50}As$
- GaAs substrate

The 50nm AlGaAs layers are intermediary layers which are helpful during the oxidation step for stabilizing the GaAs interface. Please see Section 4.6 for discussion of these results. This intermediary layer will not oxidize and will therefore serve as a high index layer for guiding light. With this in mind, the top GaAs layer was grown to be 400 nm so that the total high index layer thickness was 450 nm.

FIGURE 4.1 A scanning electron microscope (SEM) image of a randomly fractured edge of the GaAs heterostructure showing the GaAs/AlGaAs/AlAs epilayer on the GaAs substrate. The 50nm AlGaAs layers are not clearly visible due to the non uniformity of the surface.

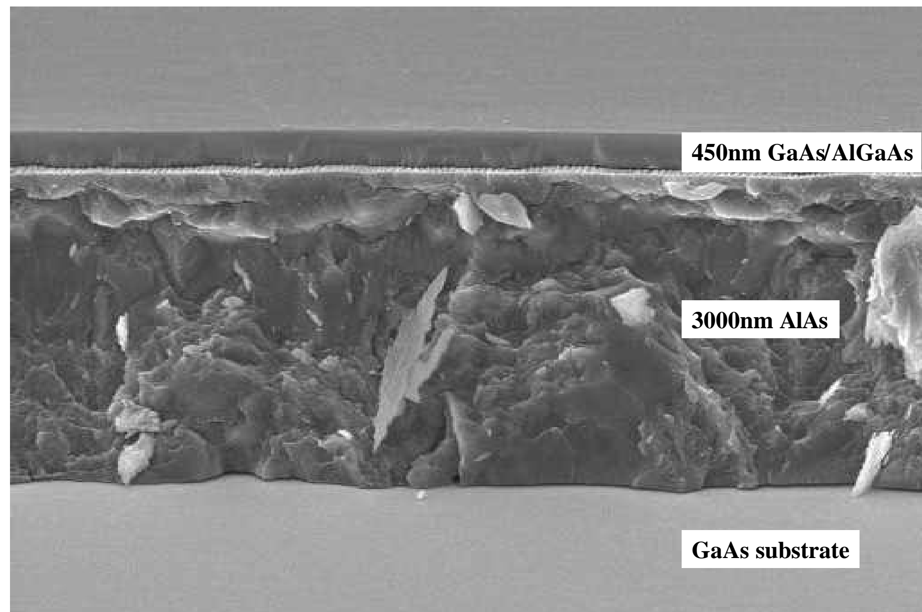

4.2 Photolithography Results

As outlined in Section 3.3, photolithography will be used to define the superprism device shape. Two photolithography steps will be used with the mask designs shown in Figure 4.2: the first using Mask 1 and the second using Mask 2.

FIGURE 4.2 Photolithography mask designs: Mask 1 (left) and Mask 2 (right). 2” Wafer outline and cross-hairs are for reference and will not be exposed. Cross and circle-shaped alignment marks are used to align the patterns from Mask 2 to the pattern exposed on the wafer using Mask 1.

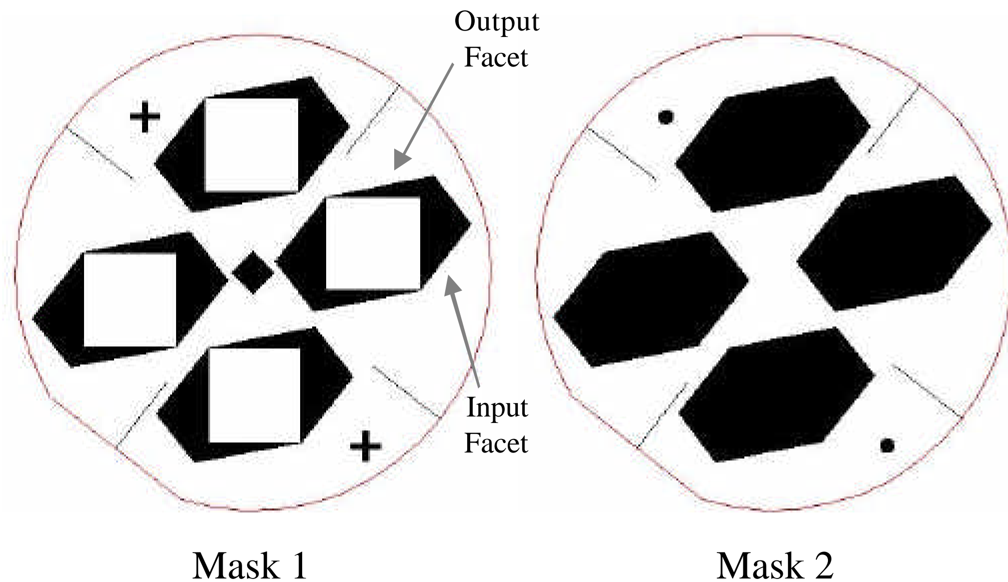

The device shape defined by the above masks differs from the shape shown in the design schematic shown in Figure 2.10. The inputs and outputs of the devices are still defined by angled facets. However, in order to optimize the number of devices per wafer, the corners of the original parallelogram shape have been trimmed. Trimming these corners allows us to pattern four device shapes per 2 inch wafer. However, the number of devices per wafer is actually eight due to the fact that each device shape has two input and two output facets on opposite sides of the photonic crystal area. Trimming the corners also helps us during the oxidation step by decreasing the lateral distance that the oxidation front needs to travel.

Mask 1 defines the device shape with an open square area. The middle of the wafer pattern has an alignment grid with a period of about 1 micron to allow for alignment of the hole pattern to the device shape during the Interference Lithography exposure step. Mask 2 covers the whole device area so that the holes exposed outside the device area can be etched away while the holes inside the device are protected. See Section 3.3 for details of these fabrication steps. Cross and circle-shaped alignment marks are used to align the patterns from Mask 2 to the pattern exposed on the wafer using Mask 1.

4.3 Interference Lithography Results

Interference lithography is used to pattern the square lattice of holes for the 2D photonic crystal. Interference lithography is a more appropriate lithography technique for this superprism design than photolithography or electron beam lithography because the hole pattern is periodic, covering a large area, and with minimum feature sizes under 1µm.

4.3.1 Basic Overview of Interference Lithography

Interference lithography (IL) allows patterning of periodic structures over a large area. The periodic pattern is formed by the constructive and destructive interference of light waves which form a standing wave at the substrate surface. This standing wave exposes a grating pattern on the substrate as illustrated in Figure 4.3.

FIGURE 4.3 In interference lithography, the standing wave formed by the interference of two light beams exposes a periodic grating on the substrate. In this schematic, the incoming waves are approximated as plane waves when in reality they are spherical.

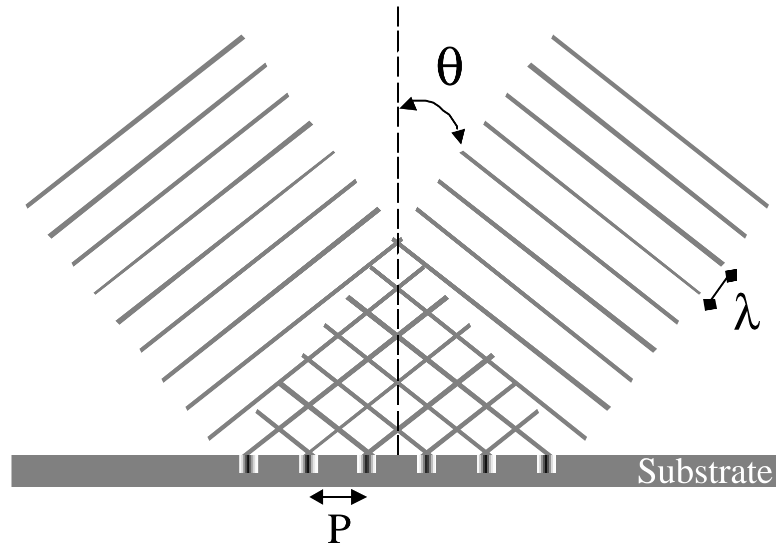

The period of the grating (P) depends on the source wavelength (λ) and the half-angle between the two beams (θ) according to:

$$P = \frac{\lambda}{2\sin\theta} \quad \text{(EQ 4.6)}$$

Two IL systems in the Nanostructures Laboratory (NSL) at MIT were investigated for patterning the photonic crystal used in this thesis: the Lloyd's mirror interferometer, and the two-beam interferometer.

4.3.2 The Lloyd's Mirror Interferometer

The Lloyd's mirror interferometer uses a broad beam of light and a mirror to create an interference pattern on the substrate as shown in Figure 4.4. The mirror sits perpendicular to the substrate surface. The interference pattern is formed by the interference between light directly incident on the substrate, and light reflected off the mirror which then hits the substrate. The period of the grating is given by Equation 4.6 with θ determined by the orientation of the mirror and substrate with respect to the incoming light.

FIGURE 4.4 Top view of the Lloyd's mirror interferometer system showing light incident upon the mirror and substrate simultaneously. The light reflected off the mirror interferes with the light directly incident upon the substrate to form a periodic pattern. The rotation stage sets the period by changing the orientation of the mirror and substrate.

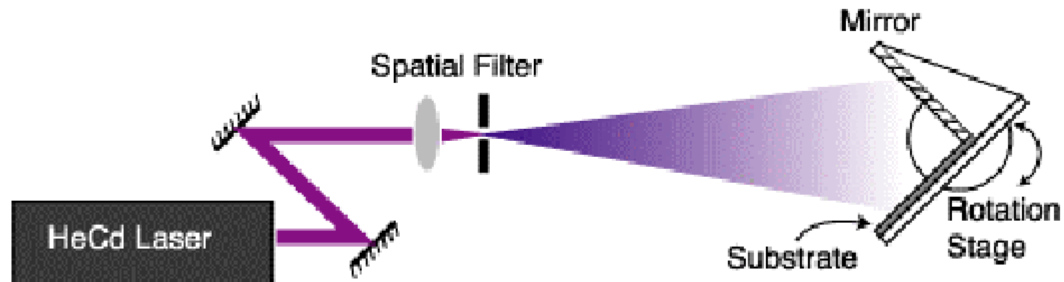

The present Lloyd's mirror system as illustrated in Figure 4.4 uses a 325 nm HeCd laser as its source. The mirror which is perpendicular to the substrate is rigidly attached to the substrate chuck via vacuum suction. A rotation stage sets the period of the grating by rotating this mirror/substrate combination. The spatial filter removes high frequency noise from the beam in order to create a clean Gaussian beam profile. A pinhole allows the beam diameter to expand so that it exposes a large area when it reaches the mirror/substrate.

FIGURE 4.5 A grating pattern in resist exposed using the Lloyd's mirror interferometer. The period is approximately 760 nm.

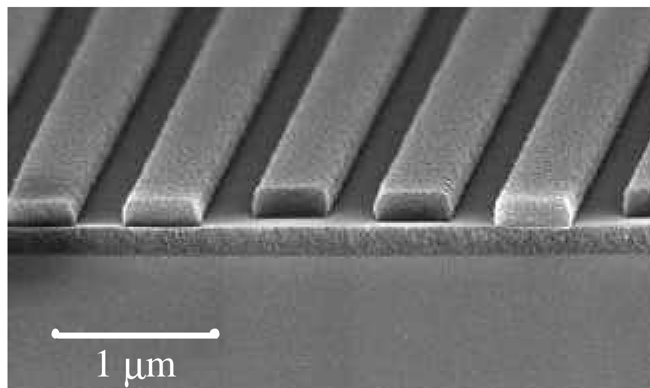

Figure 4.5 shows a 760 nm period grating exposed in negative resist using the Lloyd’s mirror interferometer. The resist pattern rests on an anti-reflective coating on a silicon substrate.

There are several advantages to the Lloyd's mirror system. Firstly, the Lloyd's mirror is fairly immune to external mechanical vibrations. Vibrations that affect the relative path length of the two interfering beams are the only vibrations that affect the pattern exposed on the substrate. Because the separation of the beam does not occur until reflection off the mirror, and the mirror is rigidly connected to the substrate, such vibrations are minimal. The result is that the relative lengths of the two beams is very stable [8]. In the two-beam IL system, which is discussed next, the splitting of the beam requires a phase-locking system to stabilize the relative path length of the beams.

A second advantage of the Lloyd's mirror system is the ease with which the period of the grating can be adjusted. Changing the period only requires changing the setting on the mirror/substrate rotation stage. No additional alignment steps are necessary.

4.3.3 The Two Beam Interferometer

Another Interference Lithography configuration is the two-beam interferometer as shown in Figure 4.6. The 325 nm beam emitted from a HeCd laser source is divided by a dielectric beamsplitter into two beams each carrying 50% of the total power. These two beams are then steered toward the substrate via two mirrors. Each beam passes through its own spatial filter to remove high frequency noise, and to expand the beam diameter. The interference pattern is formed as the two beams meet at the substrate surface.

FIGURE 4.6 The two beam Interference Lithography system used in the Nanostructures Laboratory

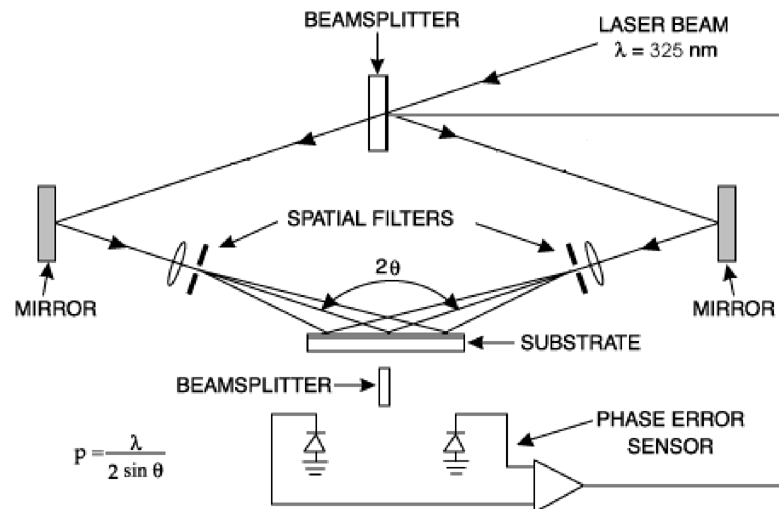

A feedback system is used to correct for relative path length differences between the two beams which may occur due to mechanical vibrations in the system. A beamsplitter above the substrate mount samples and recombines the two incoming beams as in a Mach-Zehnder interferometer. The two outputs of the beamsplitter are detected by two photodiodes which are the inputs to a differential amplifier. The differential amplifier then drives a piezomotor which adjusts the position of the first beamsplitter stage. Any change in the path length of either beam will cause the photodiode current to change. This change in current changes the position of the beamsplitter thus introducing a change in the relative path length of the two beams. By keeping the photodiode current constant, the feedback system can stabilize the phase difference between the two beams stabilizing the interference pattern at the substrate surface.

As explained earlier, the period of the grating is determined by the angle between the two interfering beams. For the 750 nm period holes of our superprism, the half-angle between the two beams must be 12.5 degrees. In order to adjust the period using the two-beam interferometer, the spatial filters must be moved and the steering mirrors must be adjusted to the appropriate angle. This adjustment process requires a realignment of the beam path through all the optical elements which is not trivial and can take several hours.

From the perspective of stabilization and flexibility of the period, the Lloyd's mirror interferometer is much easier to use. There is no need for additional feedback mechanisms to stabilize the fringe pattern nor is any adjustment process necessary to change the period. However, there are some distinct advantages that make the two-beam interferometer more appropriate for patterning the 2D photonic crystal.

4.3.4 Fabricating Photonic Crystal Grids

So far we have only discussed patterning 1D gratings using interference lithography. To fabricate 2D grids, two orthogonal grating exposures are necessary. This is accomplished by placing the substrate on a rotation stage which is rotated by 90 degrees between exposures. As discussed in Section 3.2, the tolerance on the squareness of the grid is +/- 1 degree. The resolution of the substrate rotation stage in the two beam IL system is less than one degree whereas on the Lloyd's mirror interferometer, no such stage exists and therefore the substrate would have to be manually rotated.

Examples of a number of grid exposures using the Lloyd’s mirror are shown in Figure 4.7 and Figure 4.8. By varying the exposure time, we can vary the hole size. In general, these exposure times are a function of the intensity of the laser beam at the substrate surface. When using a positive resist as in Figure 4.7, a small exposure time results in a smaller hole size. With longer exposure times, the holes become large enough to interfere with neighboring holes resulting in post structures rather than holes. When using a negative resist as in Figure 4.8, the opposite effect is observed. A longer exposure time results in a smaller hole size and short exposure times result in post structures.

FIGURE 4.7 Examples of grid exposures using the Lloyd's mirror for different exposure times. Grids are exposed in PFI 88 positive resist on silicon for (a) 2 min (b) 2min 24sec (c) 2 min 48 sec (d) 3 min 12 sec per side (the total exposure time is double). The period is approximately 750 nm for every case.

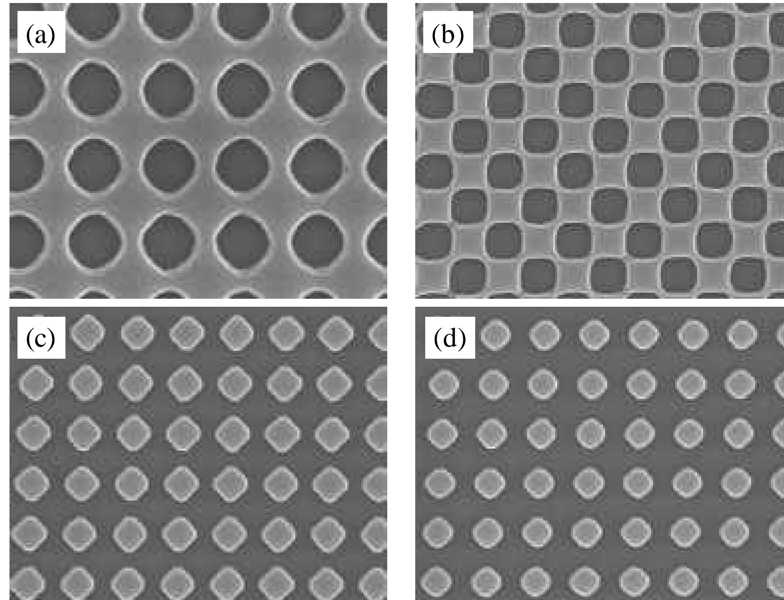

FIGURE 4.8 Examples of grid exposures in negative resist using the Lloyd's mirror for different exposure times. Grids are exposed in OKHA negative resist on silicon for (a) 1 min (b) 1 min 20 sec (c) 1 min 40 sec (d) 2 min per side (the total exposure time is double). The period is approximately 750 nm for every case.

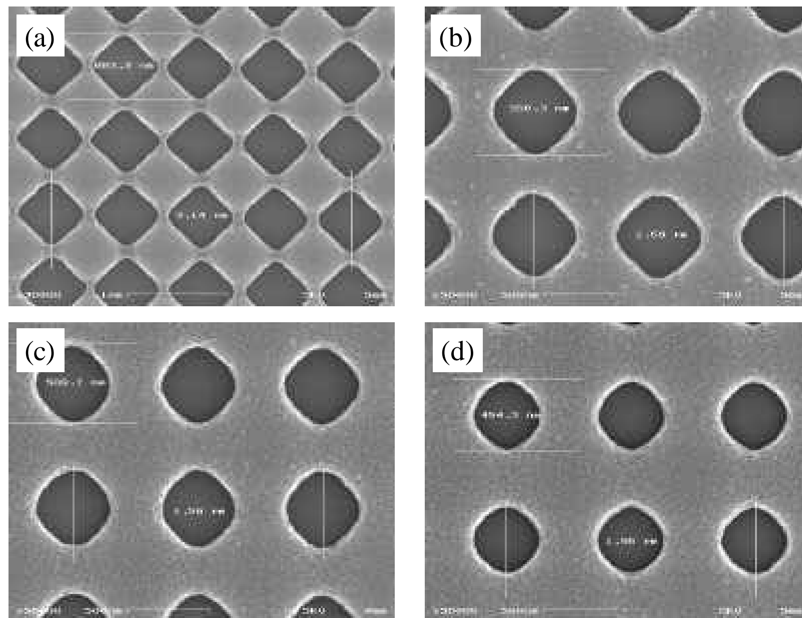

The greatest advantage of the two-beam interferometer over the Lloyd's mirror for this application is that it fixes the period of interest allowing a higher degree of repeatability between exposures. Although the multiple exposures shown above show consistently good grid patterns, the period is not consistent because the stage is reset during each exposure. Since the superprism device requires a fixed period upon which all other parameters are dependent, this repeatability is essential. Another distinct advantage of the two-beam set-up is the ability to pattern larger areas. Because the Lloyd's mirror interferes two halves of the beam diameter at the substrate surface, the exposure area is limited to one half of the beam's surface area. The two-beam system allows the full beam diameter to expose the surface therefore allowing for a greater exposure area.

4.3.5 Future Work

The exposure results presented in this thesis have all been patterned using the Lloyd's mirror interferometer. Results using the two-beam interferometer are not available since the system is not yet equipped to pattern 750 nm grids. As discussed above, one disadvantage of the two-beam system is that changing the period is quite difficult. At the present, the two-beam system in the Nanostructures Laboratory is being modified for patterning 750 nm period structures. This has involved modifying the phase locking system, building new spatial filters, and creating a new beam path for the laser beam. Future work will involve completion of these modifications and then performing exposures with the system. Testing needs to be performed to ensure that the tolerances of the design can be met. This includes determining the exposure time necessary for the correct hole size and checking that the exposed grids meet the alignment and squareness tolerances.

4.4 Substrate Preparation

Though the final superprism device is a three-layered structure consisting of GaAs, aluminum oxide, and a GaAs substrate, fabricating the device involves a number of additional layers which each have a very specific purpose. The trilayer resist stack facilitates pattern transfer from the interference lithography step, and the hard mask layer allows for deep etching of the GaAs/AlGaAs epilayers.

4.4.1 Trilayer Resist Stack

The exposure of the periodic pattern in resist using Interference Lithography can be degraded by back reflections off the substrate. Light reflected off the substrate can interfere with incident light forming an interference pattern in the vertical direction. This vertical interference pattern can result in resist sidewalls that are not perfectly straight and may also be too weak to withstand the subsequent development and etching steps.

To compensate for this effect, an anti-reflective layer (ARC) can be used below the resist layer to minimize the reflected power off the substrate. For most of our exposures, we have used BARLi ARC which is a polymer that is spun onto the wafer. Reflection at the resist/ARC boundary is dependent on the index of refraction and thickness of all the layers beneath as well as the angle of incidence and wavelength of operation. In order to mini-

mize the reflected power, we need to determine the necessary ARC thickness based on all properties of the other layers. A software simulation similar to the one used in [8] was used to determine this thickness. The program calculates the reflectivity at any boundary of the layered medium for an arbitrary layered medium. The program then generates reflectivity curves for different variables of interest.

The plot shown in Figure 4.9 shows how the reflectivity varies with ARC thickness for a layered medium. The plot can then be used to make the proper choice of materials and thicknesses. For example, using Figure 4.9, we could choose an ARC thickness of about 310 nm for a layered stack of resist, SiO_2, ARC, SiO_2 on a GaAs substrate in order to keep the reflectivity below 1% at the resist/SiO_2 boundary. The ARC is then spun onto the substrate using a variable speed spinner at the appropriate speed to ensure the desired thickness.

FIGURE 4.9 Reflectivity profile for layered medium consisting of 200nm PFI-88 positive resist, 90nm SiO_2, BARLi ARC, 250nm SiO_2, GaAs substrate.

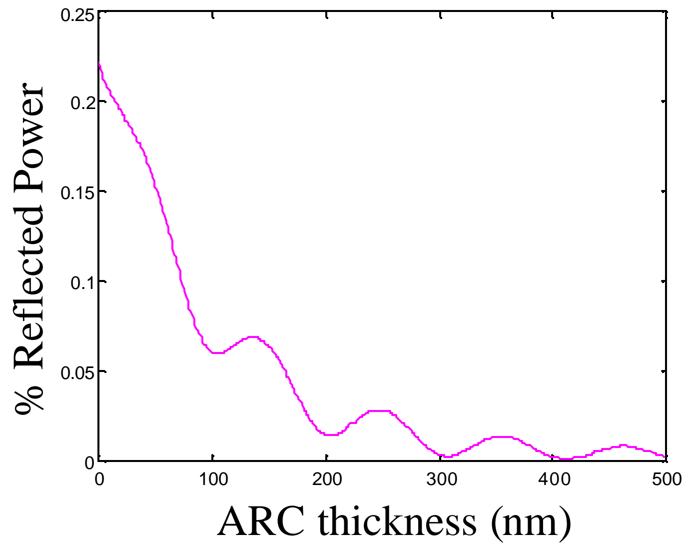

Since the resist layer often cannot withstand etching though the ARC layer, an SiO_2 interlayer is often used in between. As shown in Figure 4.10, a 90 nm evaporated SiO_2 interlayer was used to transfer the grid pattern from the resist to the ARC using reactive ion etching. In general, the interlayer should withstand the etching of the ARC layer. If a thicker ARC layer is used, the thickness of the interlayer should be adjusted. The combination of the resist, interlayer and ARC is often referred to as a "trilayer" resist stack.

FIGURE 4.10 Exposure of grid pattern using the Lloyd's mirror interferometer. (a) Grid pattern in resist with 90nm SiO_2 interlayer, 300nm ARC, and 250 SiO_2 hard mask layer on a GaAs substrate. (b) Grid pattern in the SiO_2 hard mask layer after reactive ion etching of the trilayer resist stack. A thin layer of ARC remains on top.

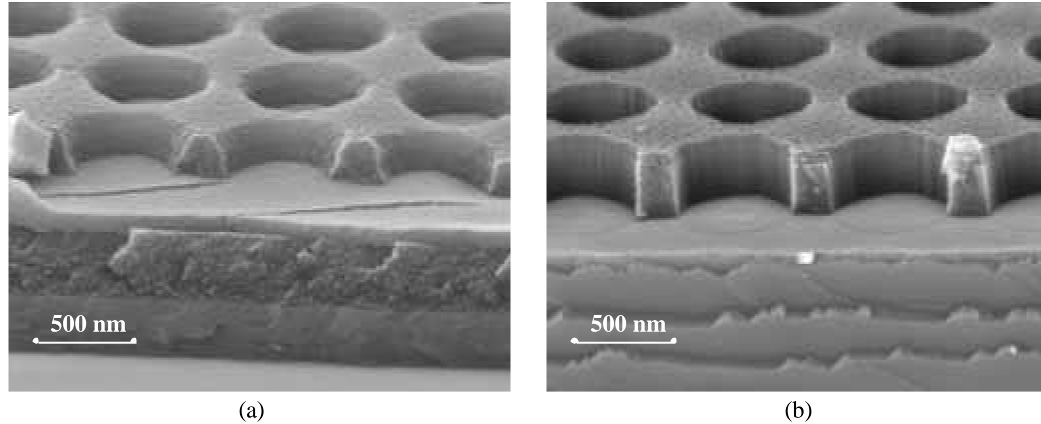

(a) (b)

Thus before any Interference Lithography exposure, the substrate must be prepared with the proper trilayer resist stack to ensure that 1) reflections off the substrate are minimized and 2) the pattern can be transferred successfully from the resist to the substrate.

4.4.2 Hard Mask Preparation

In order to etch the GaAs substrate, a hard mask layer must be used. This hard mask layer must be able to withstand the chemistry of the GaAs etch while being thick enough that it does not sputter away over the duration of the etch. Since we aim to etch the GaAs/AlAs epilayer about 1.5 microns deep, a sufficiently thick hard mask must be used.

After experimenting with different metal and dielectric masks, SiO_2 seems to be the best material for this etch. There are several ways to deposit SiO_2, including evaporation, sputtering, PECVD, among others. We experimented with each of these methods of SiO_2 deposition using the tools available to us and tried etching the GaAs layers with each type of oxide. The results of the exposure and hard mask etching steps are presented in Section 4.5 while experiments in etching the GaAs layer using these hard masks are not discussed in this thesis. However, an SEM image of two GaAs etches are presented in Section 4.5.

4.4.3 Future Work

Future work in the area of layer preparation will involve finding a consistently good hard mask layer. Though we have demonstrated success with depositing thick SiO_2 using the sputtering system in the Nanostructures Laboratory, the results are not consistently repeatable and uniformity is limited to small areas. These limits are problematic since layer thicknesses must be known for good IL exposures with small back reflection. In addition,

the surface area of our superprism device is quite large making thickness uniformity critical.

We will investigate other sources of oxide deposition. In particular, we will also investigate the use of flowable oxide as a substitute for deposited oxide. Flowable oxide such as Dow Corning's HSQ have the additional advantage of acting as an e-beam resist. Though this advantage is not directly applicable to the process steps outlined for this device, it most certainly would be advantageous for future device applications.

4.5 Reactive Ion Etching Results

Reactive ion etching is used to transfer patterns exposed during lithography steps through intermediary layers into the GaAs/AlAs epilayer. Reactive ion etching is a dry etching technique whereby ions accelerate towards the material and react with the surface. This etching method allows for highly anisotropic etching with straight sidewalls.

4.5.1 Tri-layer and hard mask etching results

Once the pattern has been exposed in resist, a number of different etching steps are necessary to transfer this pattern into the epilayer. After the interference lithography exposure, the hole pattern must be transferred from the resist layer through the SiO_2 interlayer, ARC layer, the SiO_2 hard mask layer, and finally into the GaAs/AlAs epilayer.

FIGURE 4.11 SEM image after an Interference Lithography exposure using the Lloyd's mirror interferometer. The 750 nm period hole pattern is in about 200 nm of positive resist with a 20 nm SiO_2 interlayer, 200 nm ARC layer, and 100 nm SiO_2 hard mask layer on a GaAs substrate.

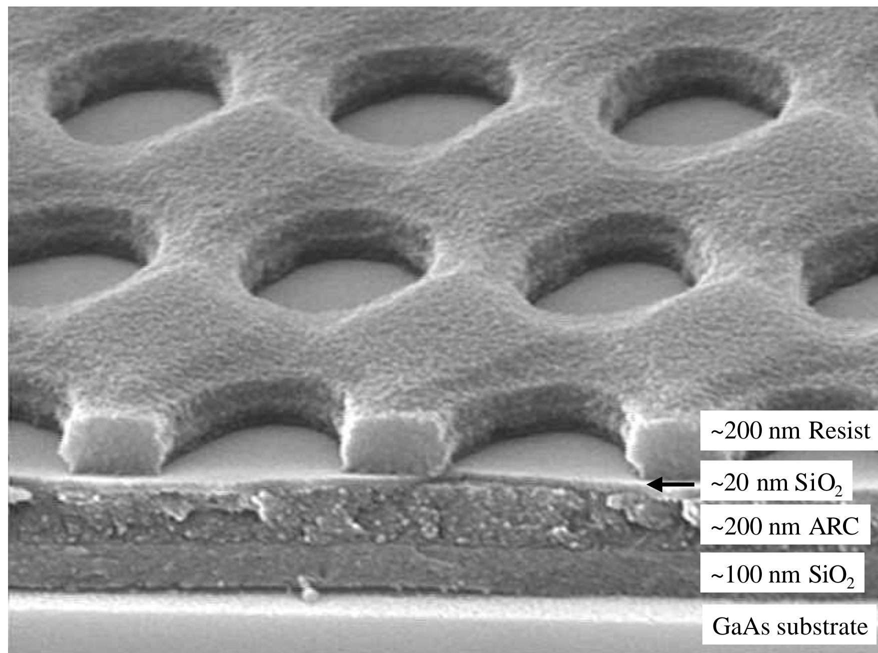

Since different materials have varying etch chemistries, different gases are used to etch each layer. SiO_2 is etched using fluorine-containing gases such as CHF_3 or CF_4, the ARC layer is etched using He/O_2, and the GaAs/AlAs epilayers are etched using BCl_3. Each etching step must performed in such a way that the mask layer is not etched simultaneously.

The details of a pattern in resist before reactive ion etching is shown in Figure 4.11. This pattern was exposed using the Lloyd's mirror interferometer in PFI 88 positive resist. The SiO_2 interlayer and ARC layers were then etched as shown in Figure 4.12. The SiO_2 was etched using CHF_3 at 10 mT, 100V, 190W for 1 min, 10 sec. CHF_3 does not etch polymers such as resist and is therefore a suitable gas for this step. The ARC layer was then etched using a 2:1 mix of He and O_2 at 10 mT, 250 V, 330 W, for 1 min, 40 sec.

FIGURE 4.12 SEM image showing holes in SiO_2 and ARC. The SiO_2 hard mask layer remains unetched. The 20 nm SiO_2 interlayer was etched using CHF_3(10 mT, 100V, 190W, 1:10) and the 200 nm ARC layer was etched using He/O_2(2:1 sccm, 10 mT, 250 V, 330 W, 1:40).

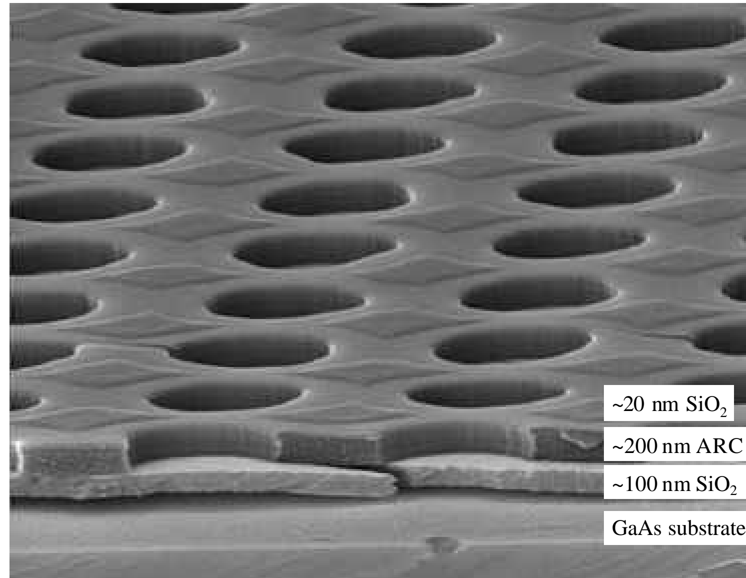

The SiO_2 hard mask was then etched using CF_4 as shown in Figure 4.13. CF_4 etches polymers such as ARC. However, since the ARC is twice as thick as the SiO_2, it will not completely etch away before the SiO_2 is etched even though the etch rate is faster. Though the etch in Figure 4.13 is not complete, it still provides us useful information by allowing us to calculate etch rates of each material. The etch rates of SiO_2 and ARC are about 30 nm/min and 40 nm/min respectively. Therefore the complete etch of the hard mask can be completed with the ARC mask in tact as long as the ARC is sufficiently thick.

FIGURE 4.13 SEM image after incomplete etching of the 100 nm SiO_2 hard mask layer using the ARC as a mask with CF_4 (10 mT, 100V, 180 W, 2:40). About 20 nm of the SiO_2 layer remains to be etched implying an etch rate of ~30 nm/min. About 95 nm ARC remains of the original 200 nm implying an etch rate of ~40 nm/min.

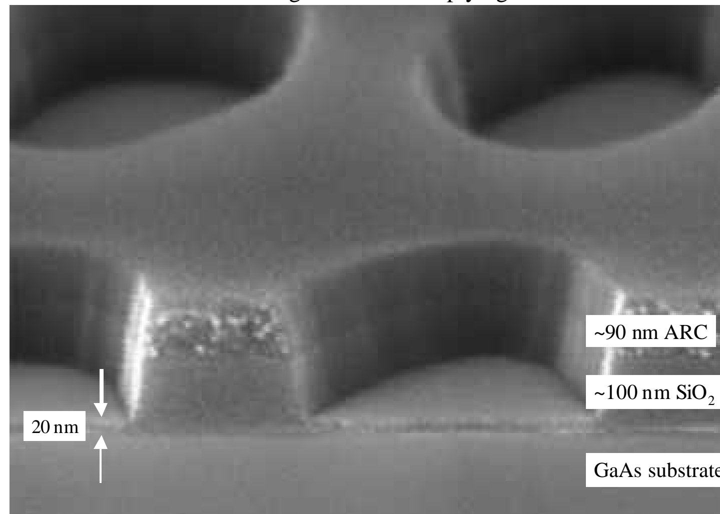

FIGURE 4.14 SEM image after etching the SiO_2 hard mask layer and He/O_2 ashing to remove the remaining ARC.

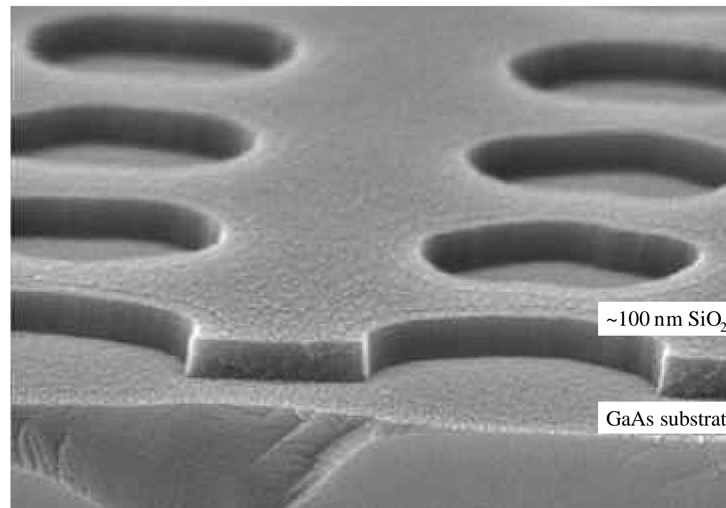

Figure 4.14 shows the completed etch of the SiO_2 hard mask layer using CF_4 and an He/O_2 ashing step which removes the remaining ARC. This hard mask was then used to etch the GaAs layer underneath using BCl_3. However, because the hard mask layer was only 100 nm, the GaAs substrate could not be etched deep enough for our design. In addition, the evaporated SiO_2 used to deposit the above hard mask was not dense enough to withstand the sputtering caused by ion bombardment at the mask surface.

We therefore tried a much thicker 500 nm SiO_2 hard mask layer which was deposited using a PECVD (Plasma Enhanced Chemical Vapor Deposition). Using a thicker hard mask layer necessitates using a thicker ARC and thicker SiO_2 interlayer in order to transfer the hole pattern through each layer. A detail of the thicker tri-layer resist stack and hard mask layer is shown in Figure 4.15.

FIGURE 4.15 Detail of a Lloyd's mirror exposure with trilayer resist stack and SiO_2 hard mask layer on a GaAs substrate.

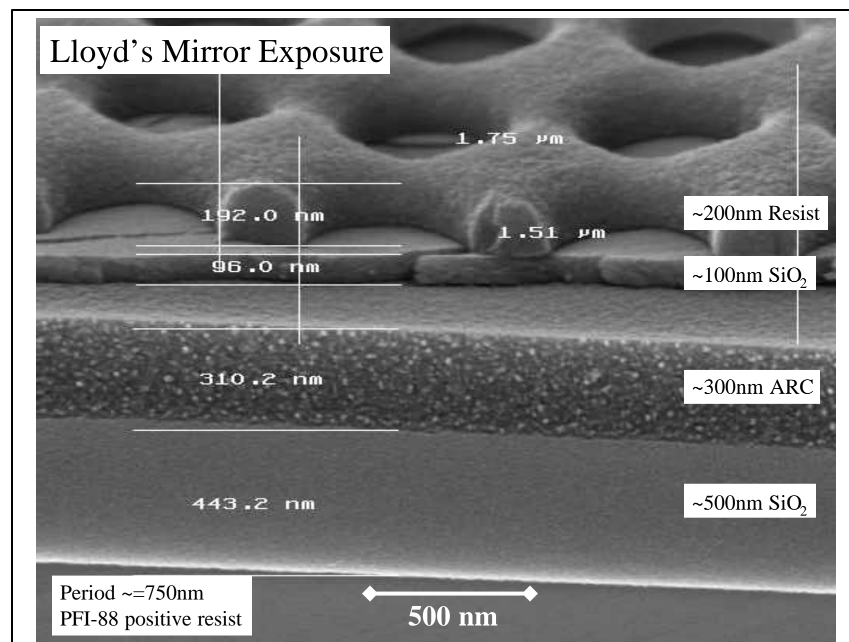

Though etching the tri-layer resist stack was straightforward, etching the SiO_2 hard mask layer demonstrated the difference between etching with CF_4 and CHF_3. Since ARC etches at a rate of 40 nm/min using CF_4, the mask would not be able to survive the 30 nm/min etching of the thicker SiO_2. As an initial trial, we first tried a 1:1 CF_4/CHF_3 mix to lower the etch rate of the ARC. The result is shown in Figure 4.16.

FIGURE 4.16 Etching the SiO_2 hard mask layer using 1:1 CF_4/CHF_3

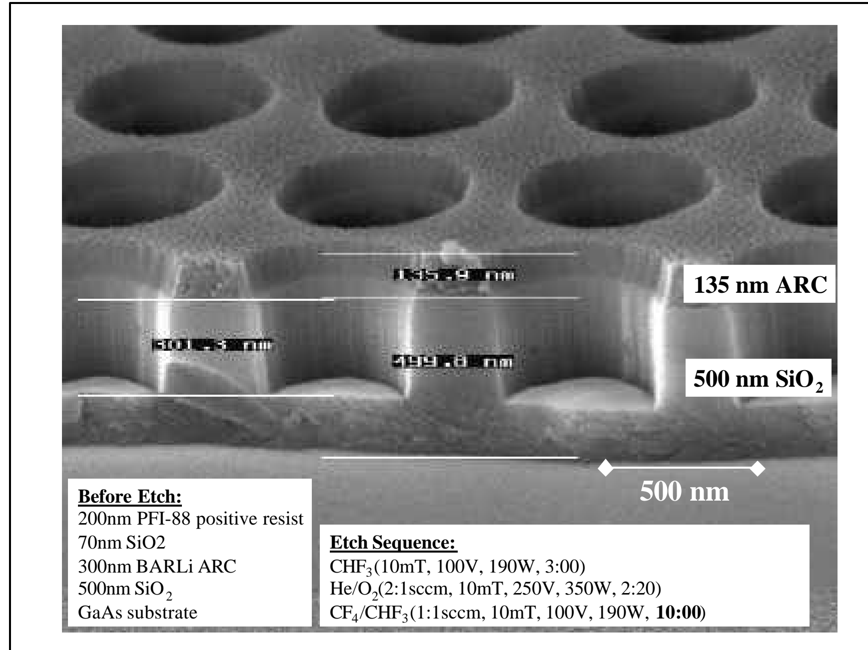

This etch illustrates that using a 1:1 CF_4/CHF_3 mix etches the ARC layer at a rate of ~17 nm/min. Since this etching rate also precludes a full etch of the SiO_2 because of the etching of the ARC mask layer, the next step was to try a pure CHF_3 etch. Though CHF_3 does not etch the ARC layer, it does sputter it. This results in a polymer build-up in the RIE chamber which may effect etch rates especially over longer length etches. The result of the pure CHF_3 etch is shown in Figure 4.17.

By comparing Figure 4.16 to Figure 4.17, we can see the difference in texture between the etched and sputtered ARC layers. The average sputtering rate was about 6.5 nm/min which is much lower than the etch rate of ARC using any CF_4 mix. With a successfully etched hard mask layer, we removed the ARC using a He/O_2 asher with the result shown in Figure 4.18.

FIGURE 4.17 Etching of the SiO_2 hard mask layer using CHF_3.

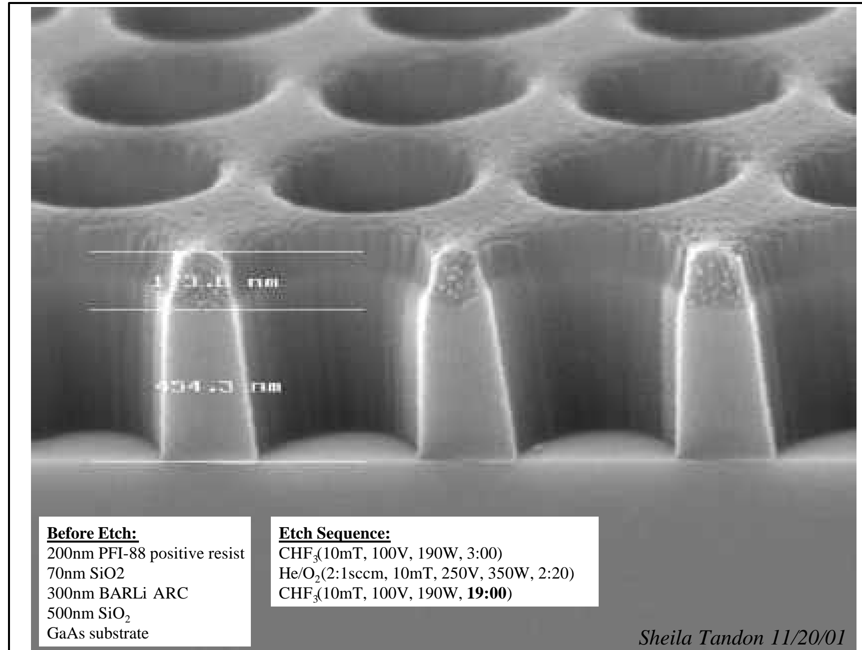

FIGURE 4.18 A 500nm SiO_2 hard mask layer after He/O_2 ashing the ARC layer

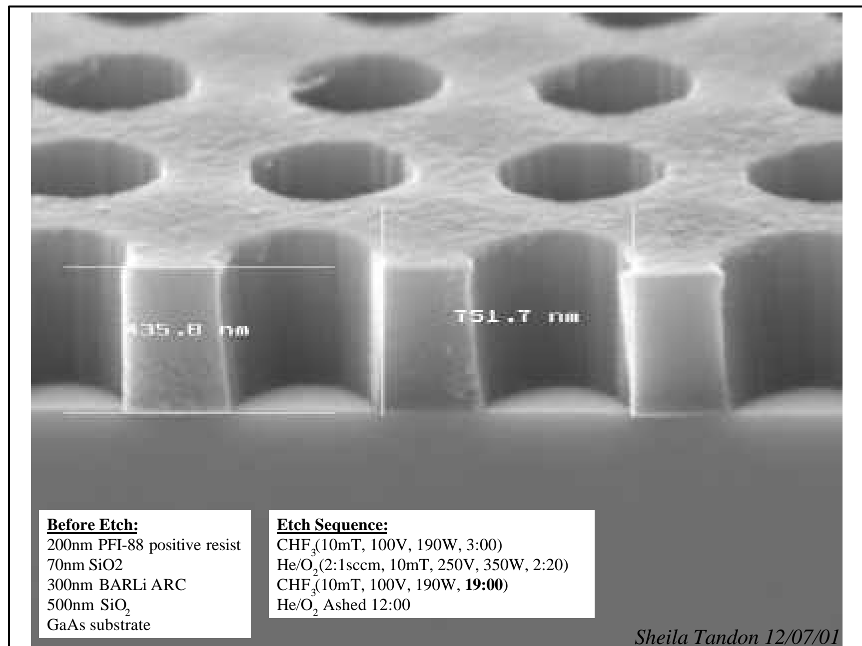

We then used this hard mask to etch the GaAs substrate using BCl_3. This oxide hard mask allowed us to etch 1.5 microns deep into the substrate as shown in Figure 4.19.

FIGURE 4.19 Results of a GaAs etch using BCl_3 (20sccm, 10mT, 60W, 500V, 20:00) with a 500 nm SiO_2 etch mask [9].

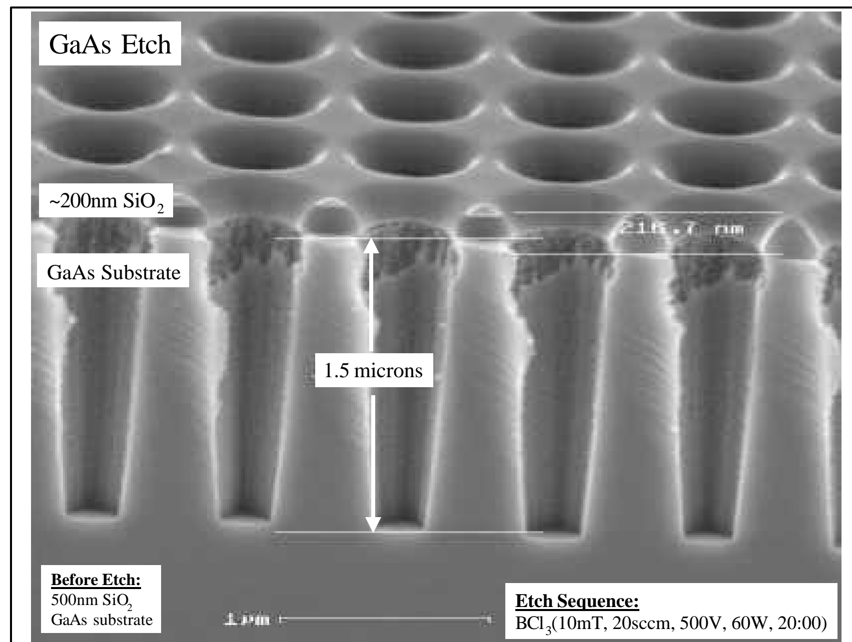

As the mask thins with sputtering, the holes in the mask become larger and the sidewalls become sloped. This sputtering of the mask results in an opening of the hole pattern in the etched GaAs as evidenced by the sidewall roughness at the top of the holes.

By changing the flow rate of the BCl_3 while keeping the pressure constant, the hole profile improved dramatically as shown in Figure 4.20. The sidewall roughness at the top of the holes is still present due to the thinning of the mask. However, the overall hole profile is much straighter with the reduced flow rate. There are several possible explanations for this. One explanation is that the lower flow rate allows the ions a longer period of time to react with the material before being purged in order to maintain constant chamber pressure.

FIGURE 4.20 Results of a GaAs etch using BCl_3 (15sccm, 10mT, 60W, 500V, 10:00) with a 160 nm SiO_2 etch mask [9].

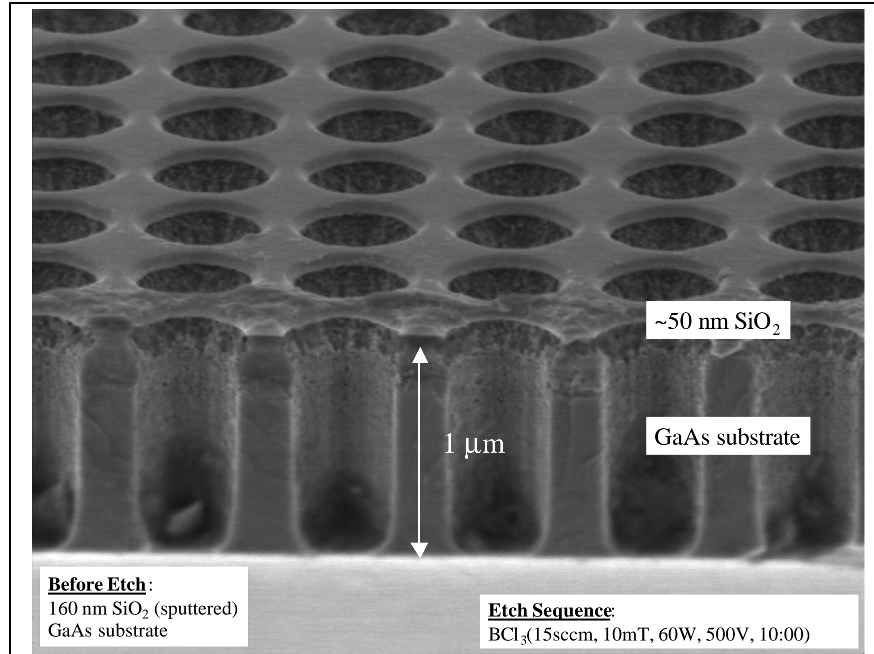

Another difference between the GaAs etch in Figure 4.19 and the etch in Figure 4.20 is the hard mask used. The etch in Figure 4.20 used a 160 nm SiO_2 hard mask which was deposited using the sputtering system in the Nanostructures Laboratory. The etch shown in Figure 4.19 used a 500 nm oxide layer which was deposited using a PECVD from an external vendor. By comparing the two etches the sputtering rate of the first etch was about 15 nm/min while the sputtering rate for the second etch was about 11 nm/min which is an improvement. This improvement could possibly be explained by the lower flow rate of the etch but may also be due to a difference in the density of the hard mask oxide.

4.5.2 Future Work

Future work will involve improving the etch quality of the GaAs by improving the side-wall profile and surface roughness. Though AlGaAs alloys also etch using BCl_3, further experiments are necessary to establish viable etch processes for this material. In addition, etch profile studies are necessary for establishing hole sizes which are in accordance with design specifications. Though the correct hole size may be exposed in the resist layer, through multiple etch steps through the various layers, this size may not be preserved. Further studies are necessary in order to adjust for any such effects.

4.6 Oxidation Results

In order to confine light in the GaAs layer of the superprism, we need to surround this layer by low refractive index material. In our superprism design, the top face of the GaAs layer borders air while the lower face borders an aluminum oxide layer. This aluminum oxide layer is created through the oxidation of an epitaxially grown $Al_xGa_{1-x}As$ layer.

4.6.1 Oxidation Experiments

The process used is a wet oxidation process identical to the one used in [10] for large scale oxidation of AlAs films. Located in an elevated temperature furnace, as shown in Figure 4.21, the film is exposed to water vapor which is carried into the furnace by an inert gas such as N_2. The temperature of the furnace is typically set between 350 and 500ºC. The rate at which the film is oxidized depends on a number of variables such as the temperature of the furnace, the aluminum content of the film, the film's thickness, and the lateral distance required for full oxidation.

FIGURE 4.21 Oxidation setup showing quartz tube which carries water vapor and N_2 into an elevated temperature furnace.

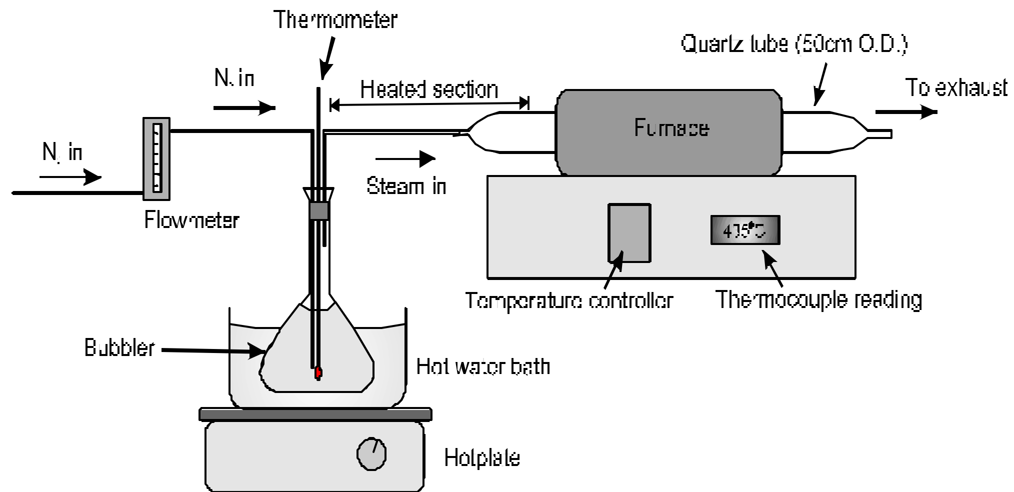

Since we are operating at a wavelength of about 3µm, our superprism design requires a low index oxide layer with a thickness of about 3µm. The longest lateral distance required for the oxidation front would be about 3mm, which is half the longest distance between the device edge and the edge of the photonic crystal square area (see Figure 4.22). Since the photonic crystal area is dominated by air holes etched deeper than the top GaAs layer, the water vapor can penetrate the exposed AlGaAs layer from this direction as well as from the input and output edges of the device.

FIGURE 4.22 Top view of superprism device shape showing the longest distance from the device edge to the photonic crystal area of ~6mm. This distance implies that the longest distance for oxidation is about half, or ~3mm.

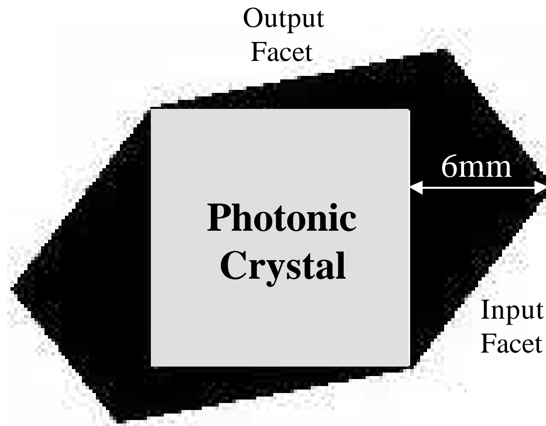

The thickness of the low index layer and the lateral oxidation distance impose a number of limitations on the oxidation process we can use for our superprism device. In general, the oxidation rate can be increased by increasing temperatures and by increasing the aluminum content of the $Al_xGa_{1-x}As$ material. The fastest oxidation they sited was a rate of about 5.5µm/min at a temperature of about 450ºC using pure AlAs (x=1). For a thickness greater than 60nm, the oxidation rate does not vary with thickness [11].

This rate implies an oxidation time of about 7.5 hours for our device--a very long oxidation time. In general shorter oxidation times are desired since long oxidations are stressful for the material and more susceptible to process variations. We can shorten this time by shortening the longest lateral distance for the oxidation front or by increasing the oxidation rate. Overcoming this limitation is the subject for future work as discussed in Section 4.6.2.

However, another important limitation to our oxidation process is the volume contraction of the material upon oxidation which is a significant factor for thicker films. As the film is oxidized at temperatures above 300ºC, the thickness of the oxide layer decreases relative to its thickness in the unoxidized state. This is due to the shrinkage in the volume per atom of the material. As Choquette, et al. observe, the volume per Al atom in AlAs is $(3.57\ \text{Å})^3$ while the volume per atom in the Al oxide is $(2.85\ \text{Å})^3$ which corresponds to a 20% linear contraction of the oxidized layers [11]. This contraction in the oxide produces stresses at the oxide/GaAs interface which can result in delamination. By increasing the Ga content of the AlAs film, we can decrease this contraction substantially. For example, Twesten, et al. cited a linear contraction of 6.7% for $Al_{0.92}Ga_{0.08}As$ [12]. However, increasing the Ga content results in a slower oxidation rate.

As an initial experiment, an oxidation was performed on a structure described in Section 4.1 consisting of 450 nm GaAs, 50 nm $Al_{0.50}Ga_{0.50}As$, 3000 nm AlAs, and 50 nm $Al_{0.50}Ga_{0.50}As$ on a GaAs substrate. The goal was to oxidize the 3000 nm AlAs layer using the 50 nm intermediary $Al_{0.50}Ga_{0.50}As$ layers to try to reduce the strain at the oxide interface upon volume contraction. Three oxidation runs were performed on cleaved samples of the above structure at temperatures of 400ºC, 430ºC, and 470ºC for 1 hour. All three runs resulted in a delamination of the GaAs epilayer, an example of which is shown in Figure 4.23. This delamination was probably caused by the large AlAs volume contraction which pulled on the AlGaAs intermediary layers. With an AlAs layer that is 3000 nm thick, a 20% linear contraction would result in a 600 nm contraction--much thicker than the AlGaAs intermediary layers and thicker than the GaAs epilayer.

FIGURE 4.23 Top view of GaAs/AlAs heterostructure illustrating delamination after an oxidation experiment at 400ºC. The delamination is shown here as a buckling of the top GaAs epilayer. The structure was 450 nm GaAs, 50 nm $Al_{0.50}Ga_{0.50}As$, 3000 nm AlAs, 50 nm $Al_{0.50}Ga_{0.50}As$ on a GaAs substrate.

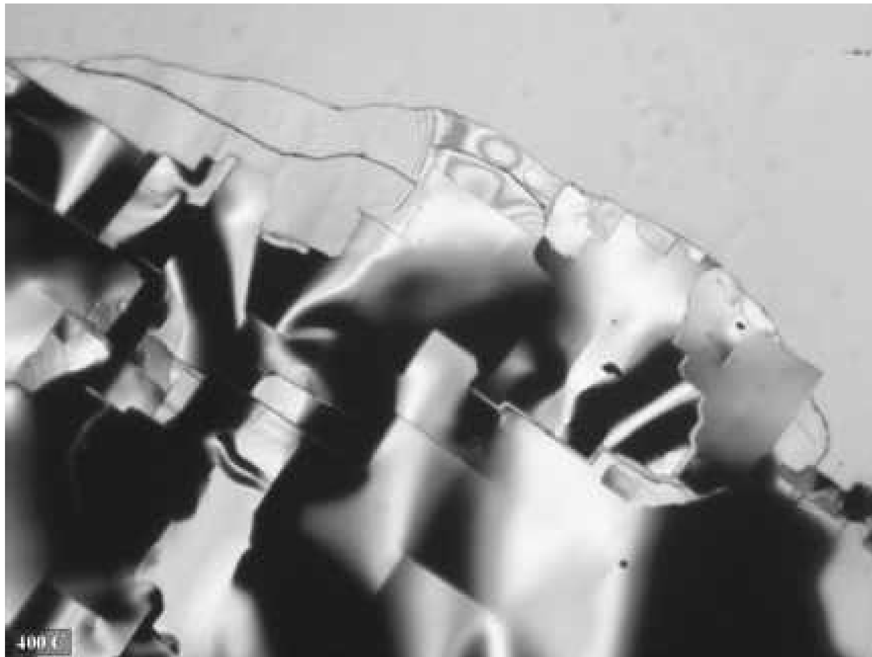

This initial experiment illustrates that oxidizing a thick layer of AlAs will not result in a stable structure. We therefore need to modify the structure in order to reduce the volume contraction while allowing for reasonable oxidation times. This will be the subject of future work.

4.6.2 Future Work

Future work on the oxidation of the superprism epilayer will involve finding a material that will allow for reasonable oxidation times while maintaining stable layer interfaces. There are a number of approaches we can experiment with.

By grading the Al content of the interface layer continuously from GaAs to AlAs we can reduce the stress at the AlAs/GaAs interface through a thin oxide transition layer. This type of transition layer is straightforward to grow epitaxially. However, even with this transition layer, the volume contraction of such a thick AlAs layer may again result in delamination.

We can shorten the total oxidation time by shortening the longest lateral distance for the oxidation front. This can be accomplished by introducing small holes in the GaAs epilayer which are etched into the AlAs layer and therefore expose this layer to the oxidation gas. The size of these holes would have to be large enough to allow for oxidation while small enough, and with a period large enough, to neglect any scattering effects during operation of the device. The effect of this solution on device operation will have to be investigated through testing of the device. Initial oxidation experiments with such holes could use 1 μm diameter holes spaced with a period of ~700 μm. These holes can be patterned using mask 1 during the photolithography step.

Using a lower Al content film would allow us to lower the effect of volume contraction on the heterostructure. Though this will result in lower oxidation rates, by using the large period of small holes in the GaAs layer, we may be able to lower the total lateral oxidation distance and therefore lower total oxidation times.

Another approach may be to use alternating thin layers of AlAs and AlGaAs to create a 3μm thick layer for oxidation. The purpose of this layered structure would be to combine the fast oxidation rates of AlAs with the stability of the interfaces between AlAs and AlGaAs while lowering the effect of volume contraction. The quickly oxidizing AlAs layers would allow for oxidation of the AlGaAs layers from the top and bottom surfaces in addition to oxidation in the lateral direction. Upon oxidation, the AlAs layers will experience a greater contraction than the AlGaAs layers. This averages out to a lower overall contraction in this structure relative to the pure AlAs case. A disadvantage of this alternative would be the difficulty in the epitaxial growth.

5.0 CONCLUSION

A superprism is an optical device which enhances the effects of a conventional prism in two ways: it disperses multiple wavelengths of light over wide angles and it allows for highly sensitive steering of a single wavelength beam.

In this Master's Thesis, a superprism device was designed focussing on realizing ultra-refraction of a single wavelength beam. A fabrication approach was then outlined, and all processing steps were investigated. Through simulations, we demonstrated that we can use the phase velocity sensitivity in a photonic crystal to amplify a beam’s direction from +/- 2 degrees at the input to +/- 30 degrees at the output for a wavelength of 3 μm. This design differs from previous work in that these superprism effects are observable in air using a simple 2D structure.

The 2D photonic crystal consists of a square lattice of air holes in GaAs surrounded by air on the top surface and low index aluminum oxide on the lower surface. The low index oxide is fabricated through a wet oxidation of an epitaxially-grown AlGaAs layer. Because of the large surface area of the device, the photonic crystal grid is patterned using interference lithography with device facets defined using photolithography. All patterns are transferred into the GaAs/AlGaAs epilayers using reactive ion etching.

Progress on all fabrication steps of the superprism has been demonstrated and the approach for future work has been identified. At the present, only minor adjustments are necessary for most fabrication steps. Successful fabrication of the device is most critically limited by the large scale oxidation necessary to create the thick low index layer. However, the direction of future experiments on this process have been outlined.

6.0 REFERENCES

[1] H. Kosaka, T. Kawashima, A. Tomita, M. Notomi, T. Tamamura, T. Sato, and S. Kawakami. "Superprism Phenomena in Photonic Crystals: Toward Microscale Lightwave Circuits." *J. of Lightwave Technology*, Vol. 17, No. 11, pp. 2032-2038, (1999).

[2] H. Kosaka, T. Kawashima, A. Tomita, M. Notomi, T. Tamamura, T. Sato, and S. Kawakami. "Self-collimating phenomena in photonic crystals." *Applied Physics Letters*, Vol. 74, No. 9, pp. 1212-1214, (1999).

[3] B. E. Nelson, M. Gerken, D. A. Miller, and R. Piestun. "Use of a dielectric stack as a one-dimensional photonic crystal for wavelength demultiplexing by beam shifting." *Optics Letters*, Vol. 25, No. 20, pp. 1502-1504, (2000).

[4] J. A. Kong. Electromagnetic Wave Theory. *EMW Publishing*, 2000. pp. 335-345.

[5] J. Joannopoulos, R. Meade, J. Winn. Photonic Crystals: Molding the Flow of Light. *Princeton University Press*, 1995, Chapters 1-4.

[6] S. G. Johnson and J. D. Joannopoulos, "Block-iterative frequency-domain methods for Maxwell's equations in a planewave basis," *Optics Express*, Vol. 8, No. 3, 173-190 (2001).

[7] Simulations performed by Chiyan Luo, MIT. Figures adapted and used with permission.

[8] Michael E. Walsh. "Nanostructuring Magnetic Thin Films Using Interference Lithography." M.S. Thesis, MIT (2000).

[9] Solomon Assefa, MIT. Figure used with permission.

[10] Alexei E. Erchak. "Enhanced Performance of Optical Sources in III-V Materials Using Photonic Crystals." Ph.D. Thesis, MIT (2002).

[11] K. D. Choquette, K. M. Geib, C. Ashby, *et al.* "Advances in Selective Wet Oxidation of AlGaAs Alloys." *IEEE Journal of Selected Topics in Quantum Electronics,* Vol. 3, No. 3, 916-926, (1997).

[12] R. D. Twesten, D. M. Follstaedt, K. D. Choquette, et al. "Microstructure of laterally oxidized $Al_xGa_{1-x}As$ layers in vertical cavity lasers," *Applied Physics Letters,* Vol. 69, 19-21, (1996).

[13] W. T. Tsang, M. Olmstead, and R. P. H. Chang. "Multidielectrics for GaAs MIS devices using composition-grades $Al_xGa_{1-x}As$ and oxidized AlAs." *Applied Physics Letters,* 34 (6), 408-410, (1979).